On the measurement of seismic travel-time changes in the time-frequency domain with wavelet cross-spectrum analysis

Shujuan Mao, Aurélien Mordret, Michel Campillo, Hongjian Fang, Robert D van Der Hilst

Geophysical Journal International

Geophys. J. Int. (2020) **221,** 550–568
Advance Access publication 2019 October 30
GJI Seismology

doi: 10.1093/gji/ggz495

On the measurement of seismic traveltime changes in the time–frequency domain with wavelet cross-spectrum analysis

Shujuan Mao [1], Aurélien Mordret [1], Michel Campillo,[1,2] Hongjian Fang [1] and Robert D. van der Hilst[1]

[1] *Massachusetts Institute of Technology, Department of Earth, Atmospheric and Planetary Sciences, Cambridge, MA,* 02139*, USA. E-mail: maos@mit.edu*
[2] *Institut des Sciences de la Terre, Université Grenoble Alpes, Grenoble, F-*38401*, France*

Accepted 2019 October 26. Received 2019 October 22; in original form 2019 May 25

SUMMARY

The spatial distribution of temporal variations in seismic wavespeed is key to understanding the sources and physical mechanisms of various geophysical processes. The imaging of wavespeed changes requires accurate measurements of traveltime delays with both high lapse-time and frequency resolutions. However, traditional methods for time-shift estimation suffer from their limited resolutions. In this paper we propose a new approach, the wavelet method, to measure the traveltime changes in the time–frequency domain. This method is based on wavelet cross-spectrum analysis, and can provide optimal time–frequency joint resolution while being computationally efficient. It can deal not only with coda but also dispersive surface waves even in the presence of cycle skipping. Using synthetic coda, we show that the wavelet method can retrieve traveltime shifts more stably and accurately than traditional methods. An application at Salton Sea Geothermal Field indicates that the wavelet method is less affected by spectral smearing and better discriminates dv/v variations at different frequencies. Furthermore, upon investigations on synthetic coda, we illustrate that the bias on dv/v measurements due to changes in source frequency content is likely to be negligible, either with traditional methods or with the new wavelet method. The wavelet method sheds lights on applications of seismic interferometry that aim to locate changes in space.

Key words: Time-series analysis; Wavelet transform; Coda waves; Seismic interferometry; Seismic noise; Wave scattering and diffraction.

1 INTRODUCTION

Temporal variations of the propagation speed of seismic waves, which are associated with perturbations in elastic properties of crustal material, provide information about temporal changes of the stress field, fluid and damages in the medium. Temporal wavespeed variations have been studied to understand the dynamic processes in various geophysical problems, including monitoring of volcanoes (Ratdomopurbo & Poupinet 1995; Sens-Schönfelder & Wegler 2006; Brenguier *et al.* 2008a; Mordret *et al.* 2010), crustal response to big earthquakes (Niu *et al.* 2003; Vidale & Li 2003; Schaff & Beroza 2004; Brenguier *et al.* 2008b, 2014; Chen *et al.* 2010; Froment *et al.* 2013; Wang *et al.* 2017), slow slip events (Rivet *et al.* 2011, 2013), and changes associated with water content (Sens-Schönfelder & Wegler 2006; Hillers *et al.* 2014; Rivet *et al.* 2015; Lecocq *et al.* 2017), tides (Yamamura *et al.* 2003; Hillers *et al.* 2015a; Mao *et al.* 2019; Sens-Schönfelder & Eulenfeld 2019) and ice sheet mass (Mordret *et al.* 2016).

Measurements of changes in seismic wavespeed can be obtained using waveforms from diverse sources, such as identical earthquakes (Poupinet *et al.* 1984; Ratdomopurbo & Poupinet 1995; Schaff & Beroza 2004; Peng & Ben-Zion 2006; Rubinstein *et al.* 2007), active source experiments (Reasenberg & Aki 1974; Yamamura *et al.* 2003; Niu *et al.* 2008; Wang *et al.* 2008) and more recently ambient noise cross-correlations (Sens-Schönfelder & Wegler 2006; Brenguier *et al.* 2008a,b; Rivet *et al.* 2011; Olivier *et al.* 2015; Mordret *et al.* 2016). With these waveforms, one can monitor the velocity changes by analysing arrival times of directly arriving waves (Leary *et al.* 1979; De Ridder *et al.* 2014; Mordret *et al.* 2014, 2019; Brenguier *et al.* 2019), or alternatively, the progressive traveltime shifts from later arriving waves, that is, coda (Niu *et al.* 2003; Schaff & Beroza 2004; Brenguier *et al.* 2008a). The latter approach, brought forth by Poupinet *et al.* (1984) and later on developed under the term coda-wave interferometry (CWI, Snieder *et al.* 2002, Snieder 2006), excels in the detection of weak velocity changes on the order of 0.01 per cent (Roberts *et al.* 1992; Weaver *et al.* 2009; Mao *et al.* 2019). This high precision comes from the fact that multiply scattered waves accumulate medium changes along its paths, which increase in length with lapse time, and are

therefore much more sensitive to perturbations than ballistic waves. Yet, the current techniques to implement CWI do not fully meet all the needs of monitoring applications.

Initially, the foremost goal of temporal change monitoring was to detect and identify perturbations, regardless of how the sources of the perturbations distribute in space. Indeed, for most previous studies on velocity changes, an important assumption is that the relative velocity change ($\mathrm{d}v/v$) before and after the perturbation is spatially homogeneous throughout the sampled medium. In this simplest case, the traveltime shifts between the current (perturbed) and reference (unperturbed) coda waveforms are expected to increase linearly with lag time t, and the relative traveltime shift ($\mathrm{d}t/t$) to be a constant. This constant, which is independent of t, yields the opposite of relative velocity change ($\mathrm{d}t/t = -\mathrm{d}v/v$).

Most media of interest are, however, not homogeneous. Furthermore, subsurface velocity changes are typically affected by a variety of tectonic and non-tectonic processes, and for each process, spatially variant changes are more common than homogeneous ones. While the aforementioned approach only gathers the average $\mathrm{d}v/v$ resulted from all the different processes, the key to understanding the physical causes and mechanisms of the different processes is to determine the spatial distribution of the changes.

One simple approach to locating the changes is by attributing the $\mathrm{d}v/v$ measured at each receiver pair either to the area in the vicinity of this pair (Brenguier *et al.* 2008a, 2014; Chen *et al.* 2010) or exactly at the two receivers (Hobiger *et al.* 2012). This, however, only provides a first-order approximation of the lateral variations of $\mathrm{d}v/v$. In fact, for inhomogeneous perturbations the traveltime shift $\mathrm{d}t$ is far from a linear function of lapse-time t, because coda waves at different lapse-times and frequencies sample perturbations that locate at different parts of the medium (Pacheco & Snieder 2005; Larose *et al.* 2010; Kanu & Snieder 2015; Margerin *et al.* 2016). Therefore, to fully image the velocity perturbations, it is crucial to investigate the variations of traveltime shifts $\mathrm{d}t$ at different frequencies and, equally important, at different lapse-times. State-of-the-art methods that can precisely procure time- and frequency-dependent $\mathrm{d}t$ are thus of primary interest.

Currently there are three types of methods to measure traveltime shifts in CWI: (1) the windowed cross-correlation method [which can be done in frequency domain (Poupinet *et al.* 1984), hereafter referred to as the doublet method, or in time-domain (Snieder *et al.* 2002)], (2) the stretching method (Lobkis & Weaver 2003; Sens-Schönfelder & Wegler 2006) and (3) the dynamic time warping method (Mikesell *et al.* 2015). Among them the doublet method and the stretching method are most commonly used in previous studies (Poupinet *et al.* 1984; Sens-Schönfelder & Wegler 2006; Brenguier *et al.* 2008a,b; Hadziioannou *et al.* 2009). Nevertheless, the critical drawback of these methods is that they are all performed in a broad frequency range and consequently lack spectral resolution. Moreover, the assumption underlying the stretching method is not valid for inhomogeneous velocity change, whereas the doublet method suffers from trade-offs between resolution, stability and computational cost.

In this paper, we propose an approach to measuring the seismic traveltime shifts with high-resolution for both time and frequency. This method is based on wavelet cross-spectrum analysis and will be referred to as the wavelet method in the rest of this paper. This wavelet method can accurately and stably measure the time-variant traveltime shifts with finer spectral resolution than existing (published) methods. These time-shift measurements with high time- and frequency-resolution are qualified for further analysis using frequency-dependent sensitivity kernels (Larose *et al.* 2010; Obermann *et al.* 2013, 2016, 2019; Kanu & Snieder 2015; Margerin *et al.* 2016; Mordret *et al.* 2019) to obtain the tomographic delineation of velocity perturbations.

In the following sections, we first review the traditional methods and introduce the new wavelet method. We then illustrate the implementation and usefulness of the wavelet method by synthetic tests in two different scenarios. Next, we investigate the robustness of different methods with respect to changes in source spectral content. We apply the wavelet method to data from a geothermal reservoir to demonstrate its feasibility on realistic data. Finally, we discuss advantages and limitations of the wavelet method.

2 METHODS FOR CODA-WAVE INTERFEROMETRY (CWI)

In CWI, the reference and current waveforms can either be generated by nearly identical sources or Green's functions reconstructed by noise cross-correlations at different times. Here we first discuss two methods that have been widely used in CWI to measure velocity change, namely, the doublet method and the stretching method, and then present the wavelet method.

2.1 Traditional approaches

2.1.1 The doublet method

A classic approach in coda wave interferometry is the doublet method, the name of which comes from its initial application on measuring $\mathrm{d}v/v$ between earthquake doublets (Poupinet *et al.* 1984). This method is also known as the Moving-Window Cross-Spectrum Technique (Fréchet *et al.* 1989; Clarke *et al.* 2011). A review of the technical details of the doublet method is given in the appendix of Clarke *et al.* (2011). Here we describe only its main idea to pave the way for later comparisons with the wavelet method.

The doublet method operates separately and repeatedly in a series of short sliding windows along the lag time. Within each window, $\mathrm{d}t$ is assumed to be constant and the current waveform segment is considered to be a shifted version of the reference. For each window, one first calculates the difference between the phase spectra of the current and reference waveform segments, that is, the phase $\phi(f)$ of the cross-spectrum of the two waveforms within this window. Then a linear fitting of $\phi(f)$ over frequency f is computed, the slope of which

yields dt in this window. The dt measured for each small window is assigned to the lapse time at the centre of that window. If the perturbation is homogeneous, dv/v is then given by the opposite of the slope of a dt versus t linear regression; if not, measurement of dt at different lapse time must be analysed further to understand the inhomogeneous velocity changes.

One problem in applying the doublet method pertains to the length of the sliding windows. On the one hand, the window length needs to be short enough, to ensure accurate measurements of dt by satisfying the assumption of constant time shift within each window, as well as to obtain good lapse-time resolution. On the other hand, the window length must be long enough to contain enough samples to correctly measure shifts between the two waveforms. Longer window lengths have also been shown to help eliminate cycle skipping (Mikesell *et al.* 2015). Therefore, the choice of the moving-window's length requires considerations on the trade-off between accuracy, time resolution, and stability of the dt measurements. In most previous studies, window lengths are chosen to be equal to (Wang *et al.* 2017; Taira *et al.* 2018) or larger than (Brenguier *et al.* 2008a; Hillers *et al.* 2015b; Mordret *et al.* 2016) the longest period of interest.

Another concern is frequency resolution. The linear fitting of $\phi(f)$ over f is executed in a pre-defined frequency range. For the stability of the regression, this range needs to be sufficiently broad since the number of sampling points in each moving-window is typically limited. For example, with window length slightly larger than the longest period, a rule of thumb is to choose a range in which the ratio of maximum frequency over minimum frequency is no less than four (Hillers *et al.* 2015b; Clements & Denolle 2018; Taira *et al.* 2018; Mao *et al.* 2019). But calculating the average dt over this broad frequency range results in low frequency resolution, which hinders the resolution of velocity perturbations' imaging, especially when dt varies significantly with frequency. Moreover, studying dt variations for different frequencies requires performing similar calculations repeatedly in multiple frequency bands, which is computationally expensive.

2.1.2 The stretching method

The stretching method considers the current waveform as a linearly stretched or compressed version of the reference with the assumption of homogeneous perturbations (Lobkis & Weaver 2003; Sens-Schonfelder & Wegler 2006). This method determines dt/t, or $-$dv/v, as the ratio by which the reference trace is dilated or compressed along time axis to maximize the cross-correlation coefficient with the current waveform. The main advantages of this method include its ability to deal with large dv/v and stability against noise in the data (Hadziioannou *et al.* 2009; Wegler *et al.* 2009). When applied to the whole waveform (Lobkis & Weaver 2003; Sens-Schonfelder & Wegler 2006), however, the stretching method does not take into consideration of the lag-time dependent changes in dt/t, and the assumption of linear stretching between two waveforms does not hold for inhomogeneous perturbations. In addition, like the doublet method, the stretching method performs in a broad frequency band and has relatively low frequency resolution. Besides, it has been argued that with the stretching method changes in source frequency content can yield spurious measurements of velocity change (Zhan *et al.* 2013), but we find different results as will be discussed in Section 4.

2.2 New approach: the wavelet method

2.2.1 Principle

Wavelet analysis is a powerful tool for studying non-stationary signals by decompositions in time–frequency space. Theoretical details of this tool can be found in Daubechies (1992) and Mallat (1999). Wavelet analysis has shown promise in various applications, including in seismology (Yomogida 1994; Gao *et al.* 1999; Kristeková *et al.* 2006; Baker 2007; Fang 2014). The ability of wavelet analysis to extract the localized time–frequency characteristics in time-variant signals makes it well-suited for our problem. Here, we restrict our use to the continuous wavelet transform (CWT), which is conducive to feature extractions with high resolution as opposed to the discrete wavelet transform. We implement our analysis using the Wavelet Toolbox in Matlab R2018a.

The wavelet transform is defined with a mother wavelet $\psi_0(\eta)$, which is a function with zero mean and localized in both time and frequency (Farge 1992; Torrence & Compo 1998). The choice of an appropriate mother wavelet will be discussed in Section 2.2.2. Considering a discrete time-series $(x_n, n = 1,\ldots,N)$ with uniform time spacing τ, its CWT is defined as the convolutions of x_n with a series of dilated and translated versions of normalized $\psi_0(\eta)$:

$$W_X(s, n) = \sqrt{\frac{\tau}{s}} \sum_{n'=1}^{N} x_{n'} \psi_0^* \left[\frac{(n'-n)\tau}{s} \right], \tag{1}$$

where s indicates how much the wavelet is scaled (dilated), n represents the time index where the wavelet is localized after translation and $(*)$ denotes the complex conjugate (Torrence & Compo 1998; Grinsted *et al.* 2004). Each scale s corresponds to a frequency f following analytical relationships that can be derived for particular wavelet functions (Meyers *et al.* 1993). At each scale the wavelet is normalized to have unit energy.

Similar to the Fourier transform, the CWT can provide power and phase information separately. The amplitude, $|W_X(s, n)|$, is the square root of local power and the angle, $arg(W_X(s, n))$, is the local phase at each lapse-time and scale (or frequency). In the time–frequency space of W_{XY}, the region potentially affected by edge-effect artefacts is called the cone of influence (COI, Mallat 1999). The COI can be calculated

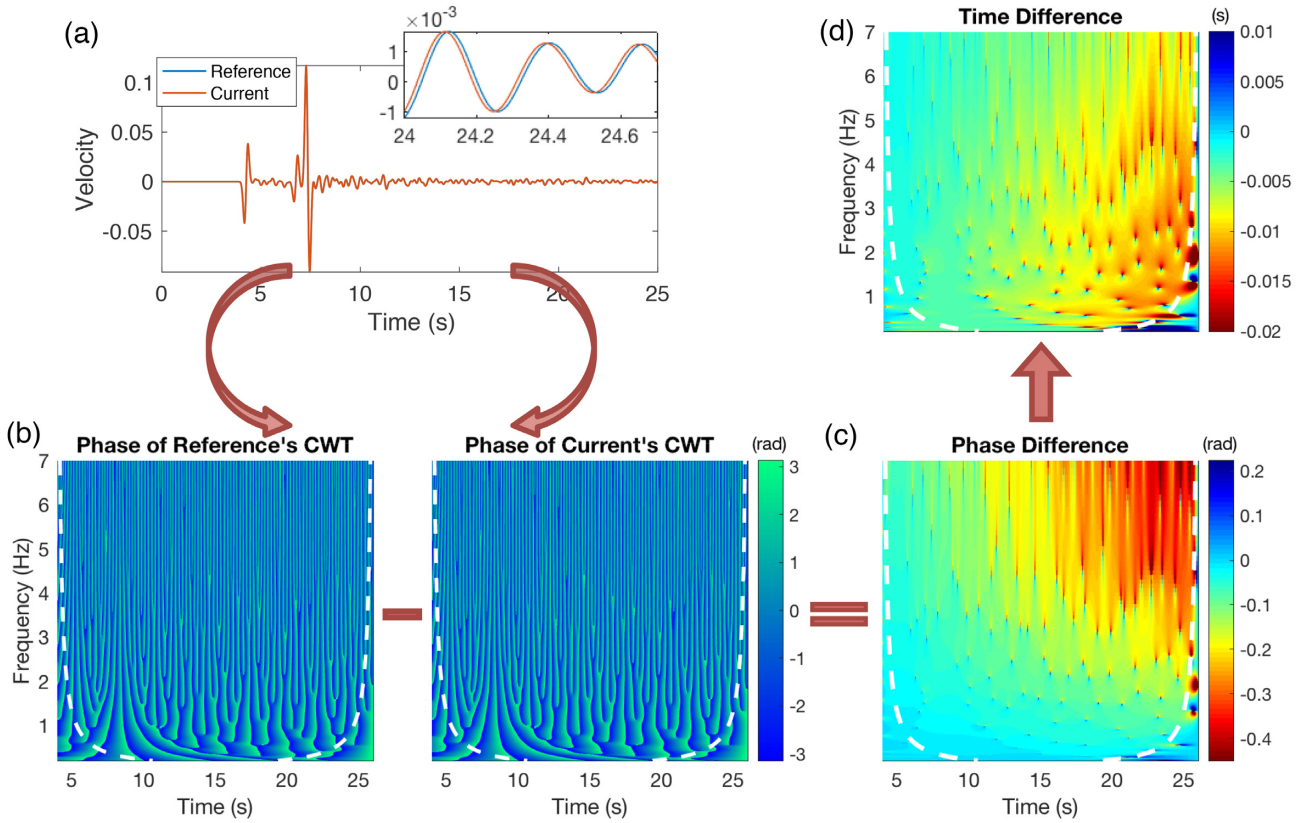

Figure 1. A conceptual illustration of the algorithm of the wavelet method to measure traveltime shifts. (a) The reference and current waveforms. (b) The phase of the two CWTs in the time–frequency domain. (c) The 2-D phase difference between the two CWTs. (d) The time difference $\delta t(f,\ t)$ in the time–frequency domain. The anomalous points (in blue-ish or orange-red colour) in c and d are due to measurement error at low local power locations corresponding to yellowish points in Fig. 3(c). White dashed lines in b–d indicate the cone of influence (COI), denoting the area where edge effects become significant.

following Torrence & Compo (1998) as spectral area where the dilated wavelets extend beyond the edges of the signal. Beyond COI the edge-effects are negligible, but within COI the wavelet spectrum should be interpreted with caution.

In seismic interferometry, typically, a reference time sequence and a current one (x_n and y_n, respectively) with similar waveforms are compared (Fig. 1a). The cross wavelet transform (XWT), or the wavelet cross-spectrum, of x_n and y_n is defined as:

$$W_{XY}\ (s,n) = W_X\ (s,n)\, W_Y^*(s,\ n)\,. \tag{2}$$

The $|W_{XY}(s,\ n)|$ is the amplitude product of the CWTs of x_n and y_n, and $arg(W_{XY}(s,\ n))$ is the phase difference between the two:

$$|W_{XY}\,(s,\ n)| = \ |W_X\,(s,\ n)| \cdot |W_Y\,(s,\ n)|\,, \tag{3}$$

$$arg\ (W_{XY}\,(s,\ n)) = \ arg\,(W_X\,(s,\ n)) - arg\,(W_Y\,(s,\ n))\,. \tag{4}$$

By transforming parameters s and n into f and t, respectively, $arg(W_{XY}(s,\ n))$, the phase of the wavelet cross-spectrum, gives $\phi_{XY}(f,\ t)$ (Fig. 1c), which is the phase difference between the two waveforms at each frequency f and each lapse-time t. Finally, the time-shift $\delta t(f,\ t)$ over the whole time–frequency space is given by:

$$\delta t\ (f,\ t) = \frac{\phi_{XY}\,(f,\ t)}{2\pi f}. \tag{5}$$

One can then derive the velocity changes with different spatial patterns from $\delta t(f,\ t)$ (Fig. 1d). We will discuss how to select high-quality $\delta t(f,\ t)$ measurement and refer to several possible ways of deriving the spatial distribution of velocity perturbations in Section 2.2.2. But more details of this part of the problem are beyond the scope of the wavelet method. In this paper, we will show examples of velocity change estimation with only simple models in Section 3–5.

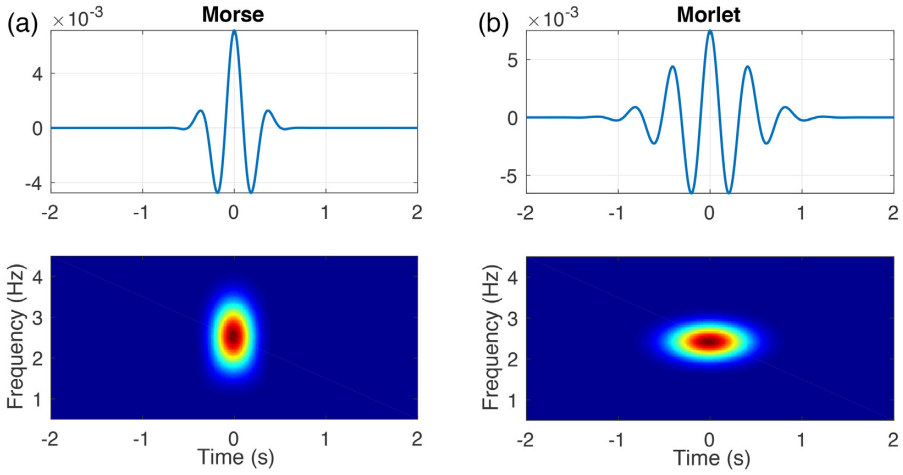

Figure 2. (a) The real-valued time-series (upper panel) and time–frequency distribution (lower panel) of the Morse wavelet defined in eq. (9) with $[P,\ \gamma] = [3, 10]$. (b) The same as in a but of the Morlet wavelet defined in eq. (7) with $\omega_0 = 6$.

2.2.2 Implementation

Choice of the mother wavelet function The CWT does not prescribe a specific mother wavelet function, and an appropriate mother wavelet needs to be chosen depending on the goals of the application. For the measurement of $\delta t(f,\ t)$, the following attributes are required:

(i) The wavelet should have a shape that reflects the characteristics of the time-series. In other words, smoothly varying functions are more suitable for seismograms than boxcar-like functions. One of the most widely used mother wavelets is the Morlet wavelet, which was first proposed in exploration seismology (Morlet *et al.* 1982a,b). The Morlet mother wavelet consists of a plane wave modulated by a Gaussian, defined in the time domain as:

$$\psi_0\ (t) = \pi^{-1/4}\ e^{i\omega_0 t} e^{-t^2/2}. \tag{6}$$

(ii) The wavelet needs to be analytic, that is, its Fourier transform is zero for all negative frequencies. The analytic Morlet mother wavelet is defined in frequency domain as:

$$\hat{\psi}_0\ (\omega) = \pi^{-1/4}\ H(\omega)\, e^{-(\omega-\omega_0)^2/2}, \tag{7}$$

where $H(\omega)$ is the Heaviside step function:

$$\begin{cases} H\ (\omega) = 1\ for\ \omega > 0, \\ H\ (\omega) = 0\ for\ \omega \le 0. \end{cases} \tag{8}$$

(iii) Different wavelets have different 2-D spreads in time–frequency space, resulting in different time and frequency resolutions. Consider another wavelet, for example, the generalized Morse wavelet (Lilly & Olhede 2009),which is defined in the frequency domain with parameters P and γ as:

$$\hat{\psi}_{P,\gamma}\ (\omega) = H(\omega)\, \omega^{\frac{P^2}{\gamma}} e^{-\omega\gamma}. \tag{9}$$

The analytic Morse wavelet, for example with $[P,\ \gamma] = [3, 10]$ (Fig. 2a), has better time resolution but poorer frequency resolution than the analytic Morlet wavelet with $\omega_0 = 6$ (Fig. 2b). The uncertainty principle theorem sets a lower bound on the area of the time–frequency spread of any wavelet:

$$\Delta t\, \Delta\omega \ge \frac{1}{2}, \tag{10}$$

where Δt and $\Delta\omega$ are the wavelet's time and frequency bandwidths respectively [see Mallat (1999) for precise definitions of the time and frequency bandwidths].

Hence, there is always a trade-off between time and frequency localization in choosing an appropriate wavelet. How to compromise between the two depends on specific applications. For instance, the Morlet wavelet (Fig. 2b) is a better choice for dv/v applications where there is a large gradient along the frequency axis, whereas the Morse wavelet (Fig. 2a) is more suitable when high time-resolution is needed. Unless otherwise noted, in the remainder of this paper we use the Morlet mother wavelet (with $\omega_0 = 6$).

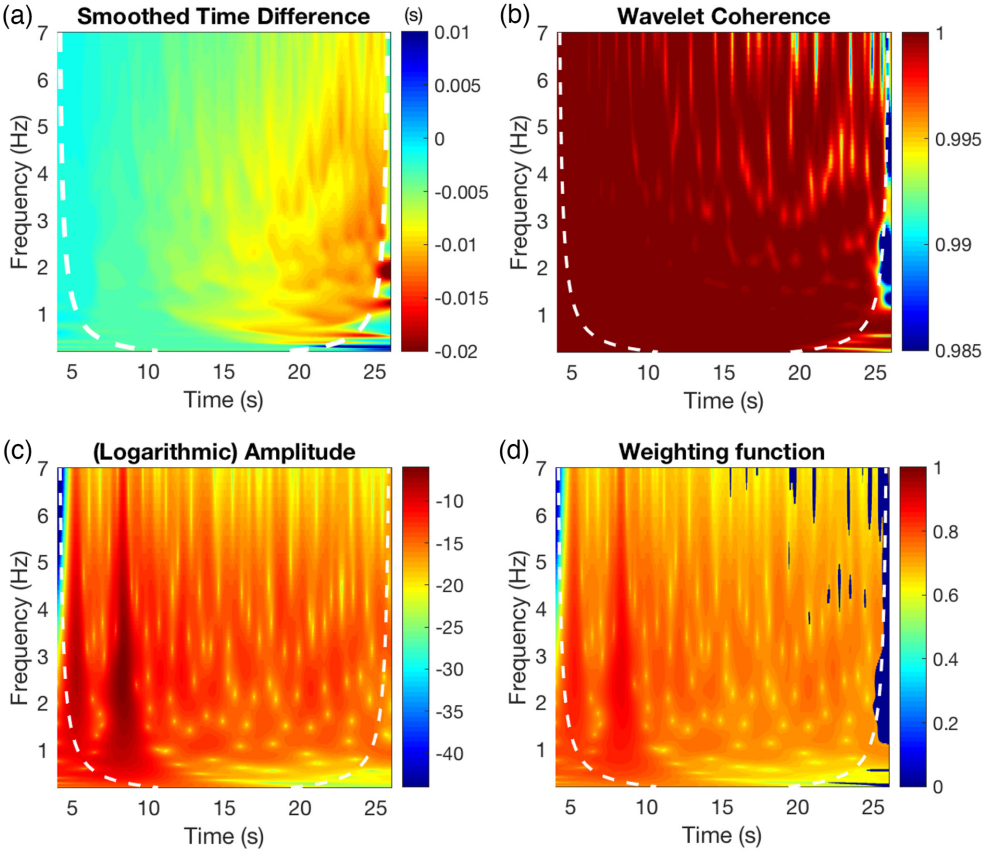

Figure 3. (a) The smoothed version of the 2-D time-shifts in Fig. 1(d). (b) The wavelet coherence corresponding to Fig. 1 as defined in eq. (11). (c) The amplitude in logarithmic scale of the wavelet cross-spectrum W_{XY} for waveforms in Fig. 1. (d) The weighting function as defined in eq. (12), taking into account the wavelet coherence in b and the amplitude of cross-spectrum in c.

Wavelet coherence Wavelet coherence is a useful quantity that measures how coherent the two waveforms are in the time–frequency space. It is defined as:

$$R^2_{XY}\ (s,n) = \frac{\left|\mathcal{S}\left\{s^{-1}W_{XY}\,(s,n)\right\}\right|^2}{\mathcal{S}\left\{s^{-1}|W_X\,(s,n)|^2\right\}\cdot\mathcal{S}\left\{s^{-1}|W_Y\,(s,n)|^2\right\}}, \tag{11}$$

where $\mathcal{S}\{\cdot\}$ is a smoothing operator in both time and scale, which is necessary to avoid coherence values being identically one at all times and frequencies (Liu (1994); similar to the Fourier cross-spectrum coherence). The exact smoothing protocol is dependent on the choice of wavelet. For the Morlet wavelet used in this paper, we choose a boxcar window (with 3 scales length) in the scale direction and a Gaussian window of width 's' ($e^{-t^2/(2s^2)}$) in the time direction (Torrence & Webster 1999).

The wavelet coherence defined above is real-valued within [0, 1] over the time–frequency domain. The measured $\delta t(f,\ t)$ are physically meaningful only where the two waveforms are similar enough. Thus, $\delta t(f,\ t)$ measured at a time and frequency where $R^2_{XY}(f,t)$ falls below a given threshold should be discarded. Figs 3(a) and (b) show the smoothing and corresponding wavelet coherence for the $\delta t(f,\ t)$ in Fig. 1(d).

Weighting of δt(f, t) Depending on the signal-to-noise ratio, the phases of the two waveforms may not be well-defined at the time and frequency where the local power of the waveforms is low compared to the noise. A natural way to improve the reliability of measurements is to use a weighting function based on the amplitude of the wavelet cross-spectrum $|W_{XY}(f,\ t)|$ (Fig. 3c), which reflects the local power of the two waveforms. Indeed, the anomalous points of $\phi_{XY}(f,\ t)$ (Fig. 1d) and $\delta t(f,\ t)$ (Fig. 1d) coincide with the locations of low local power in Fig. 3(c), where the measurement errors are large. Combined with the coherence and normalized in the time–frequency domain, the weighting function $w(f,t)$ defined as (Fig. 3d):

$$\begin{cases} w\,(f,t) = 0, & \text{for } R^2_{XY}\,(f,t) < \text{ threshold} \\ w\ (f,\ t) = \log\left(|W_{XY}\,(f,\ t)|\right)/\max_{f,t}\log\left(|W_{XY}\,(f,\ t)|\right), & \text{otherwise} \end{cases} \tag{12}$$

can be used to weigh the $\delta t(f,\ t)$ in further analysis on $\delta t(f,\ t)$ using coda waves.

For direct waves with large amplitudes, a more suitable choice is (Fichtner *et al.* 2008):

$$\begin{cases} w(f,\ t) = 0, \quad \text{for } R^2_{XY}(f,t) < \text{ threshold} \\ w(f,\ t) = \log\left(1 + |W_{XY}(f,\ t)|\right) / \max_t \log\left(1 + |W_{XY}(f,\ t)|\right), \quad \text{otherwise} \end{cases}, \tag{13}$$

where $\max_t$ means the maximum value along the time axis for each f, indicating a normalization at each frequency. This weighing reduces the dominance of large spectral amplitudes and accounts more for information at lower levles of spectral power.

In this study, we apply the weighing defined in eqs (12) and (13) for synthetic test in Section 3.1 (using coda waves) and Section 3.2 (using direct waves), respectively.

Imaging velocity changes in space from δt(f, t) From the measurements of the 2-D traveltime shifts $\delta t(f,\ t)$, various approaches can be used to image the spatial distribution of velocity changes depending on the models of perturbations.

For depth-dependent velocity perturbations, one way is to use coda waves and compute linear regressions of $\delta t(f,\ t)$ verses t for each single f to get $-\delta t/t$, or dv/v, at different depth. An alternative way using surface waves (Wu *et al.* 2016; Mordret *et al.* 2019) is to first calculate the relative changes of Rayleigh wave phase velocity $\frac{\delta C}{C}(f)$ at different frequencies by $-\frac{\delta t(f)}{t_{phase}(f)}$, then invert for the shear wave velocity changes at different depth $\frac{\delta \beta}{\beta}(z)$ using the depth sensitivity kernel $K(f,\ z)$.

For scenarios incorporating fully inhomogeneous velocity perturbations, the recently developed coda wave sensitivity kernels (Pacheco & Snieder 2005; Larose *et al.* 2010; Obermann *et al.* 2013, 2016, 2019; Planès *et al.* 2014; Mayor *et al.* 2014; Kanu & Snieder 2015; Margerin *et al.* 2016) can be applied directly on $\delta t(f,\ t)$ to retrieve the full spatial distribution of velocity changes.

2.2.3 A summary of main steps

The main procedure of the wavelet method is summarized in the following steps:

(i) Choose an appropriate mother wavelet function.
(ii) Compute the continuous wavelet transforms (CWT) of the reference and the current waveforms (Fig. 1b).
(iii) Calculate the wavelet cross-spectrum W_{XY} from the two CWTs, and obtain its phase spectrum $\phi_{XY}(f,\ t)$ (Fig. 1c).
(iv) Divide $\phi_{XY}(f,\ t)$ by $2\pi f$ at each frequency and lapse-time to get $\delta t(f,\ t)$ (Fig. 1d, assuming no cycle skipping).
(v) Define a weighting function for $\delta t(f,\ t)$.
(vi) Use $\delta t(f,\ t)$ to derive velocity changes (beyond contents of the wavelet method).

3. SYNTHETIC TESTS

In this section, we illustrate the performance of the wavelet method with synthetic seismograms. First, we use synthetic coda simulated for velocity models before and after a homogeneous perturbation, and compare dv/v measurements using the wavelet and doublet methods. Secondly, we use synthetic surface waves, incorporating frequency-dependent perturbations, to show how the wavelet method deals with dispersion and cycle skipping.

3.1 Homogeneous dv/v measured from synthetic coda

We present an example using elastic simulations of synthetic coda for a simple case of homogenous dv/v in a heterogeneous medium, to illustrate how the wavelet method is implemented and to compare against the measurements with the classic doublet method.

In this case, we adopt a 2-D elastic medium with adequate scattering, but without intrinsic attenuation. This 2-D heterogeneous medium is designed following Frankel & Clayton (1986) and Obermann *et al.* (2013), containing a 81.92 by 40.96 km homogeneous background model on which random heterogeneities are superimposed (Figs 4a and b). In the reference (unperturbed) medium, the background model has a uniform P-wave velocity $v_{P0} = 6\ \text{km s}^{-1}$, a S-wave velocity determined by $v_{S0} = v_{P0}/\sqrt{3}$ and a density of $\rho_0 = 0.23 \cdot (3281 \cdot v_{P0})^{1/4}$ (Gardner *et al.* 1974). In this simulation, the grid spacing is 0.08 km, the time step is 0.002 s, and the source is a Gaussian wavelet with a time bandwidth of 0.72 s. The heterogeneities are produced by a von-Karman type autocorrelation as in Obermann *et al.* (2013) and the correlation length is 2 km, which is comparable to the dominant wavelength. The current model is obtained by uniformly increasing the velocity in the reference model by 0.05 per cent, that is, a constant dv/v of 0.05 per cent over the whole medium. We generate the synthetic seismograms using a 2-D finite difference code (Li *et al.* 2014), with a free surface at the top and absorbing boundaries for the other three sides.

The synthetic seismograms for lapse-time 0–40 s are shown in Fig. 4(d), with a zoom-in view of part of the coda in Fig. 4e). We use coda from 18.65 s (about three times of S arrival time) to 35 s to compute traveltime shifts, with both the doublet and the wavelet methods. The coda amplitude spectra are shown in Fig. 4(f). We choose five frequency bands, 0.6–1.2 Hz, 0.75–1.5 Hz, 1.1–2.2 Hz, 1.6–3.2 Hz and 2.4–4.8 Hz. With the doublet method, the dt are calculated for each of the five bands, with window lengths comparable to the Morlet wavelet (with $\omega_0 = 6$) in each frequency band. With the wavelet method, we calculate the dt with high frequency resolution, but only plot measurements averaged over each frequency band to facilitate comparisons with results using the doublet method. Displayed in Figs 5(a) and

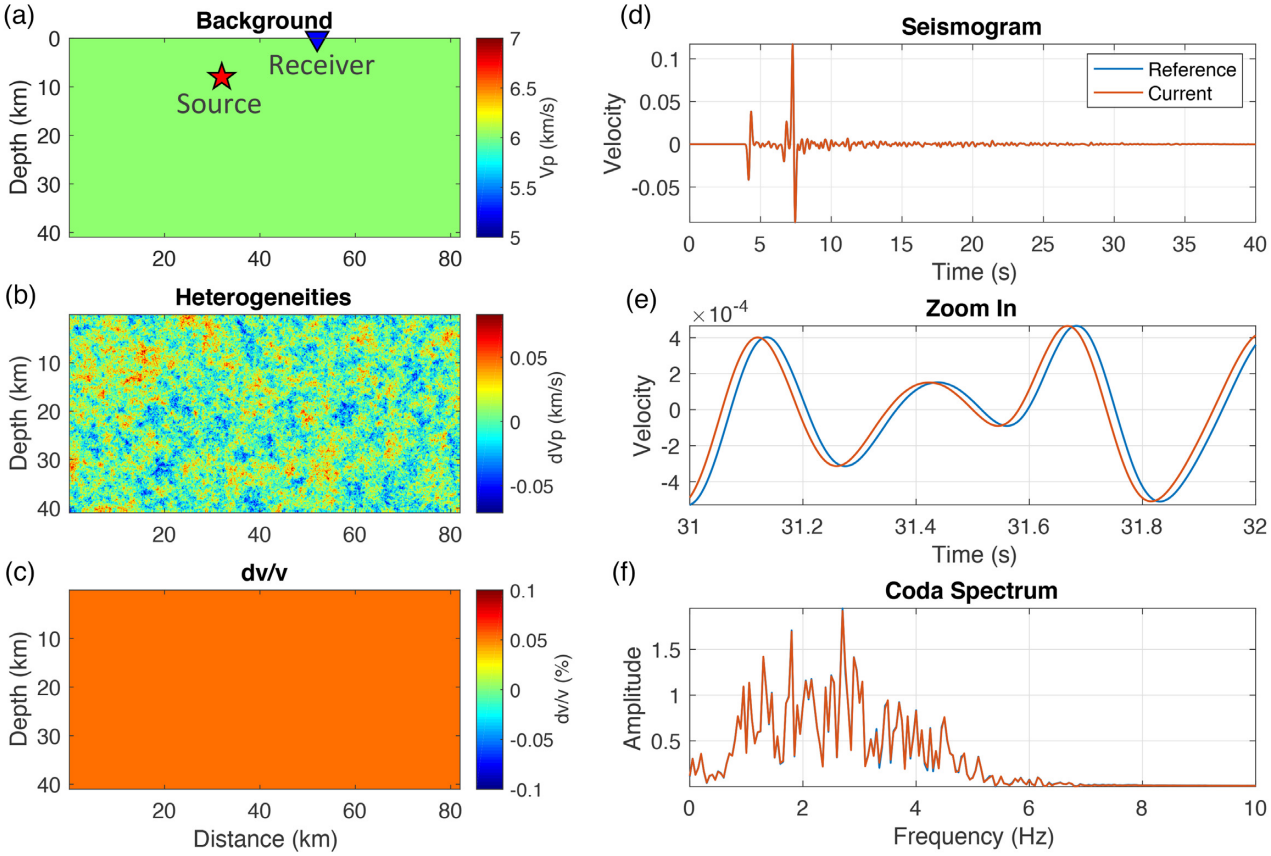

Figure 4. The models and synthetics for coda wave simulations. (a) The uniform background velocity model. (b) The random heterogeneities. The final reference velocity model used for simulations is the sum of a and b. (c) The relative difference, that is, dv/v, between the current and reference models. (d) The synthetic seismograms by 2-D elastic finite difference simulations. (e) A zoom-in view of the synthetic coda, showing slight difference between the current and the reference. (f) The spectra of codas between 18.65 and 35 s of the synthetic seismograms.

(c) are dt along lapse-time for each frequency bands, and Figs 5(b) and (d) the probability distribution of the derivations of measured dt from modelled values, using the two methods, respectively.

In this example with the simple model of a uniform velocity change, dt calculated with both methods (Figs 5a and c) reveal evident and consistent linear trends for all frequency bands. Measurements from the doublet method (Figs 5a and b), however, exhibit random but non-negligible deviations from the linear trend. We note that the measurement errors can vary a lot depending on the choice of the window function in the doublet method. In contrast, the dt measured with the wavelet method (Figs 5c and d) manifest only minute fluctuations, suggesting better stability all along the lag-time.

By linear regressions of dt over lapse time t, in Fig. 5(e) we compare the dv/v calculated for each frequency bands using the two methods, as well as at much finer frequency resolution using the wavelet method. Both methods give measurements very close to the true value (0.05 per cent). Fig. 5(e) demonstrates that the wavelet method provides better frequency resolution than the doublet method. In addition, dv/v measured with the wavelet method is more accurate and reliable up to high frequency as long as the coda contains sufficient energy (in this case, ∼4.5 Hz, as shown in Fig. 4f). Above ∼4.5 Hz, dv/v measurements become systematically smaller than the true value, because the phase measured at these frequencies are contaminated by that at lower frequencies due to spectral leakage. We note that applying spectral whitening prior to the d t calculations can help reduce the bias resulted from fluctuations in waveforms' spectral power.

3.2 Frequency-dependent dv/v measured from dispersive waves

This synthetic example shows the applicability of the wavelet method to dispersive ballistic waves for measuring frequency-dependent velocity changes. It also demonstrates how the wavelet method can deal with cycle skipping. This way of resolving the time- and frequency-dependence and cycle skipping of phase misfit is also useful for velocity model iterations in imaging and tomography (Fichtner *et al.* 2008).

In addition to coda, one can also use direct waves to monitor velocity changes (Leary *et al.* 1979; De Ridder *et al.* 2014; Mordret *et al.* 2014, 2019; Toyokuni *et al.* 2018; Brenguier *et al.* 2019). The advantages of using ballistic waves come from their well-understood propagation characteristics, which facilitate the retrieval of the spatial distribution of velocity changes. In this example, we use surface waves which can be well-reconstructed from ambient noise cross-correlations (Shapiro & Campillo 2004; Yao *et al.* 2006).

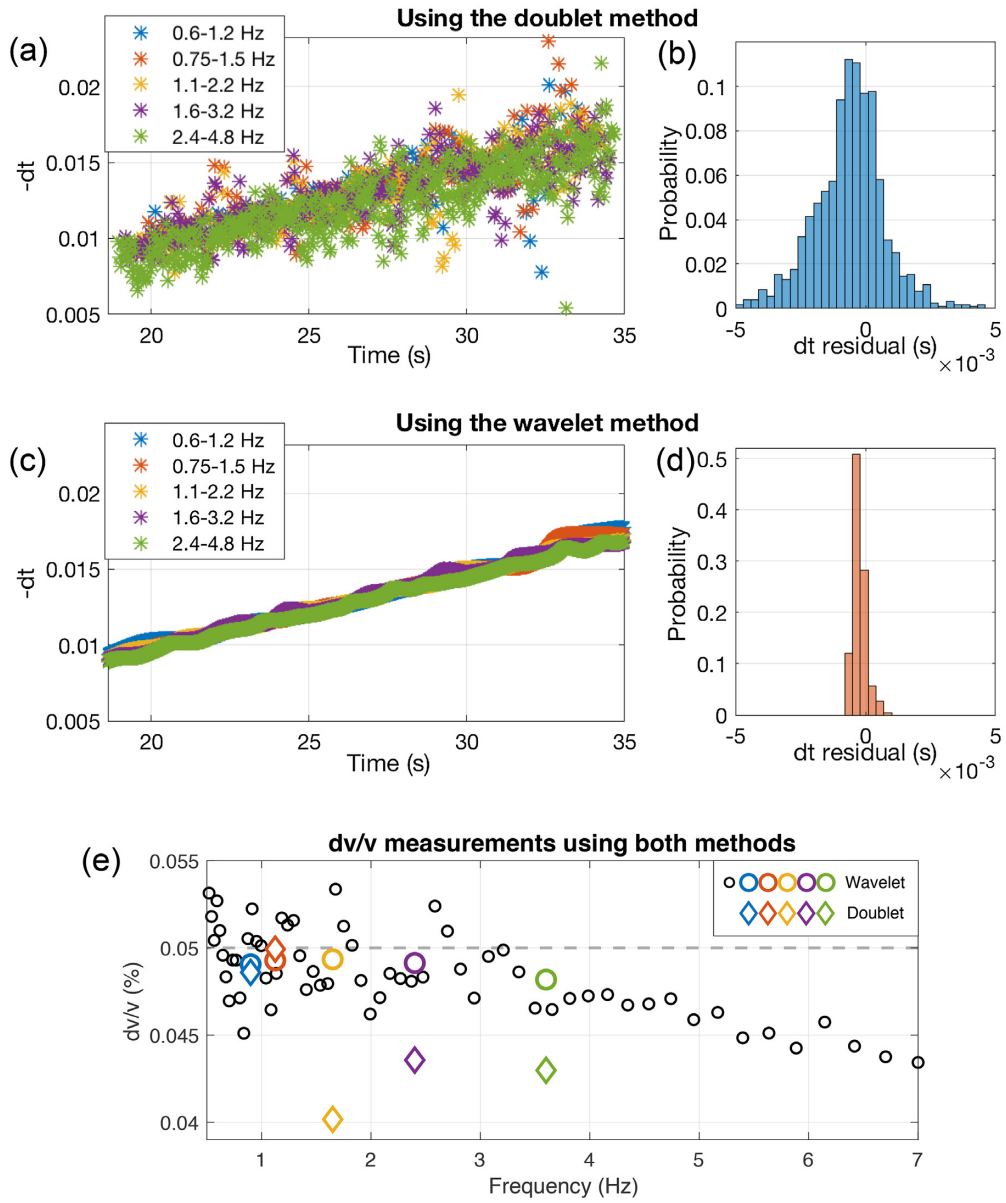

Figure 5. Using the doublet method: (a) the time-shifts as a function of lapse-time measured for five bands and (b) the probability distribution of all dt measurement residuals from the model. Using the wavelet method: (c) measurements of the time-shift along lapse-time averaged over each frequency bands and (d) the probability distribution of all dt measurement residuals from the model. (e) dv/v measured using the doublet method (in coloured diamonds) and the wavelet method (in coloured circles) for five frequency bands (the colours for each bands correspond to those in a and c), and using the wavelet method at each frequencies (in small black circles). The dashed grey line denotes the model value of dv/v.

The difficulties of utilizing surface waves, however, lie in dispersion and the presence of cycle skipping. The doublet method is not suitable for this situation, but the wavelet method can deal with both challenges. The 2-D phase difference $\phi_{XY}(f,\ t)$ measured with the wavelet method allows unwrapping along t axis (for each f), which helps mitigate the cycle skipping problem. Meanwhile, the 2-D measurements allow the range of t to vary arbitrarily at each f, as opposed to the doublet method in which only the same t range can be used across the whole frequency band.

We illustrate these advantages using synthetic dispersive surface waves (Fig. 6a), which [similar to the example in Fichtner *et al.* (2008)] are analytically defined by:

$$u_{\text{ref}}\ (x,t) = \int_{\omega_{\min}}^{\omega_{\max}} \cos\left[\omega\left(t - \frac{x}{c_{\text{ref}}\,(\omega)}\right)\right] \mathrm{d}\omega, \tag{14}$$

$$u_{\text{cur}}\ (x,t) = \int_{\omega_{\min}}^{\omega_{\max}} \cos\left[\omega\left(t - \frac{x}{c_{\text{cur}}\,(\omega)}\right)\right] \mathrm{d}\omega, \tag{15}$$

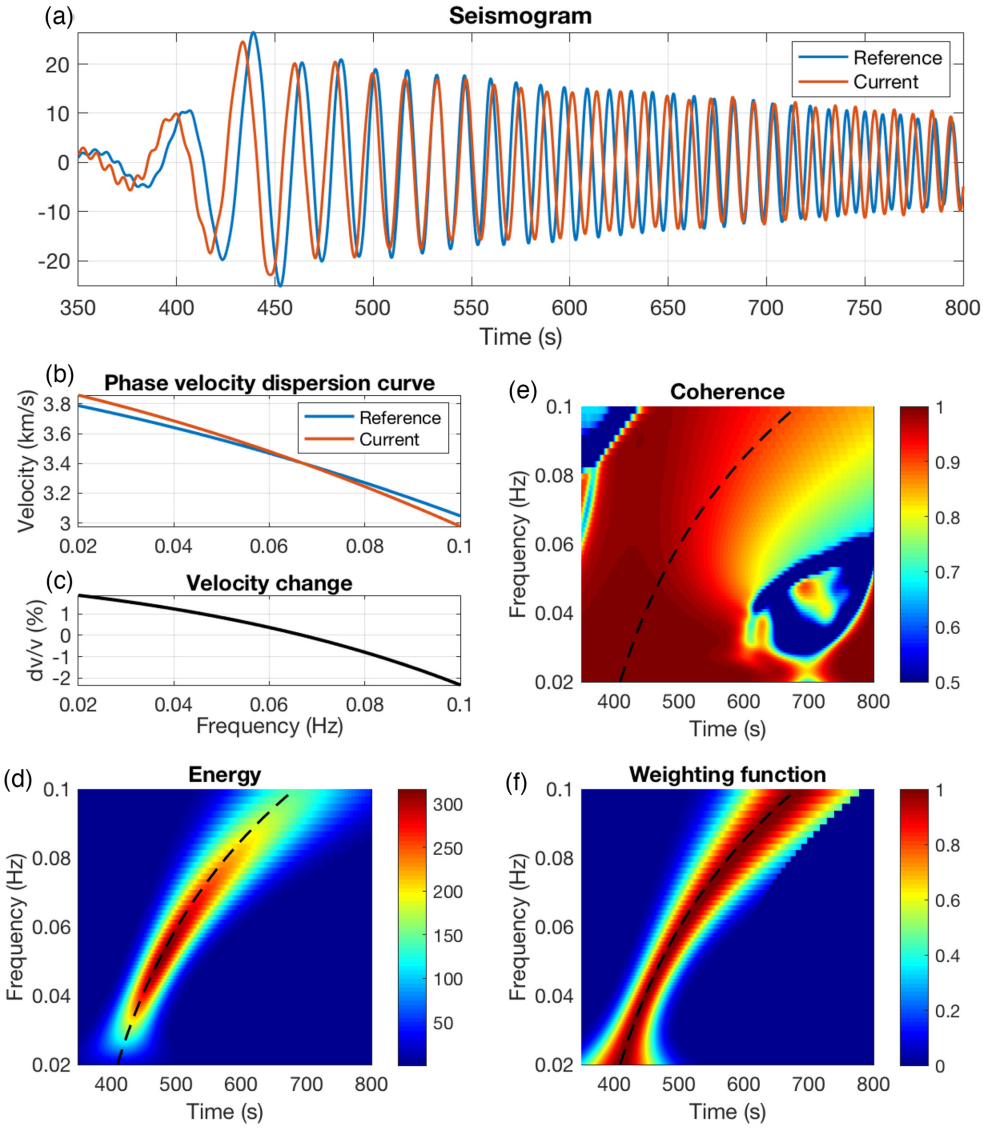

Figure 6. (a) The reference (eq. 14) and the current (eq. 15) synthetic seismograms calculated with two dispersion curves in b. (b) The reference (eq. 16) and current (eq. 17) phase velocity dispersion curves. (c) The relative difference (dv/v) between the two phase velocities. (d) The amplitude, (e) the wavelet coherence, and (f) the weighing function of the wavelet cross-spectrum of the reference and the current synthetics. Black dashed lines in d–f are the theoretical group velocity dispersion curves calculated by differentiating the reference phase velocity dispersion curve (eq. 16). The high amplitude region in d, obtained from the wavelet (cross) transform, naturally gives the group velocity dispersion.

where the epicentral distance $x = 1500$ km, $\omega_{\min} = \frac{2\pi}{10}$ rad s^{-1}, and $\omega_{\max} = \frac{2\pi}{50}$ rad s^{-1}. $c_{\text{ref}}(\omega)$ and $c_{\text{cur}}(\omega)$ are two slightly different phase velocity dispersion curves defined by:

$$c_{\text{ref}}\ (\omega) = -0.8\omega^2 - 0.87\omega + 3.91, \tag{16}$$

$$c_{\text{cur}}\ (\omega) = -\omega^2 - \omega + 4. \tag{17}$$

These two dispersion curves are displayed in Fig. 6(b) and the relative difference between the two in Fig. 6(c). The velocity difference varies with frequency, mimicking realistic situations where the velocity perturbations are not homogeneous but vary with depth. The synthetic seismograms (Fig. 6a) display evident dispersive features. It is shown that the current and reference waveforms are nearly in phase at ∼550 s; before this time the current is advanced relative to the reference and vice versa after. After ∼600 s, cycle skipping between the two is observed.

We calculate the wavelet cross-spectrum W_{XY} of the two synthetics; the amplitude of W_{XY} (eq. 3), the wavelet coherence (eq. 11), and the weighting function (eq. 13) are shown in Figs 6(d)–(f), respectively. The large amplitude in Fig. 6(d) from the wavelet (cross) transform,

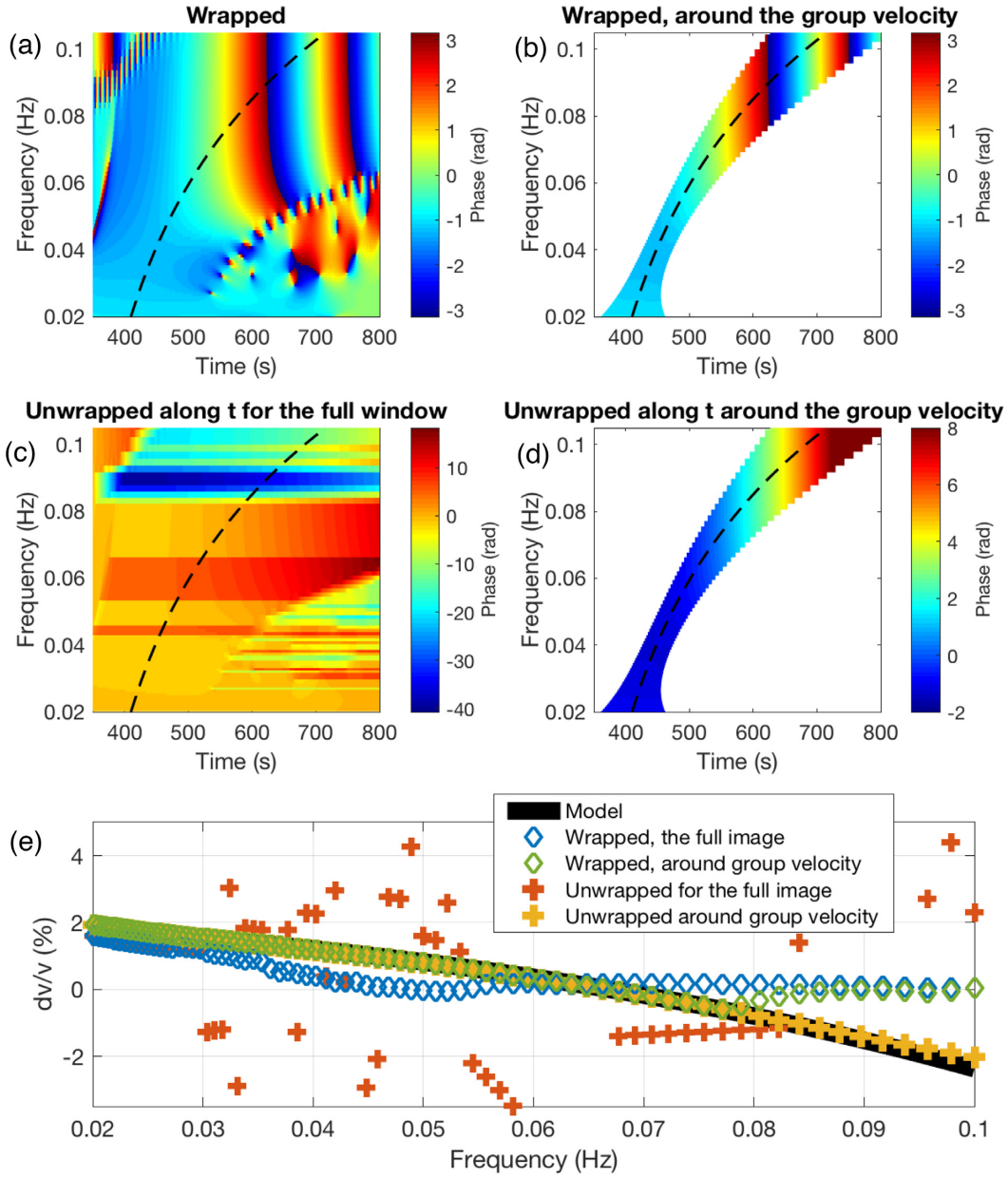

Figure 7. (a) The wrapped phase (within $[-\pi,\ \pi]$) of the wavelet cross-spectrum W_{XY} of the two synthetics in Fig. 6(a). (b) The same as in a but only shown in the area with high weighting values based on Fig. 6(f). (c) The phase after unwrapping along time axis for the full window from 350 to 800 s. (d) The phase after unwrapping along the time axis only within the area of high weighting values based on Fig. 6(f). Black dashed lines in a–d denote the theoretical group velocity dispersion. (e) The model dv/v and the measurements using phases shown in a–d.

and therefore the high weighting area in Fig. 6(f), naturally gives the group velocity dispersion [the theoretical dispersion curves in black dashed lines in Figs 6(d)–(f) are calculated by differentiating the reference phase velocity dispersion curve in eq. (16)].

Fig. 7(a) displays the phase $\phi_{XY}(f,\ t)$ of the cross-spectrum W_{XY}, which is also the phase difference between the two seismograms, ranging $[-\pi,\ \pi]$. Dividing $\phi_{XY}(f,\ t)$ by $2\pi f$ gives $\delta t(f,\ t)$, and linear regressions of $\phi(f,\ t)$ over lapse-time t in each row give dv/v for each frequency f. The dv/v inferred in this way (blue diamonds, Fig. 7e) exhibits non-negligible discrepancies from the modelled dv/v (bold black line, Fig. 7e).

These discrepancies come from the aforementioned two problems of using $\phi(f,\ t)$ in Fig. 7(a). First, due to the dispersion, using the full lapse-time window uniformly across the whole frequency range leads to the involvement of inauthentic phase measurements. Instead, only phase at $(f,\ t)$ with high weighting values, as shown in Fig. 7(b), should be used. Secondly, directly taking the phase of the W_{XY} between $[-\pi,\ \pi]$ causes biases due to cycle skippings at late arrivals. Fortunately, the 2-D $\phi(f,\ t)$ map makes it possible to obtain the continuous phase change for each frequency f by unwrapping along the lapse-time t. Fig. 7(c) displays the phase unwrapped along t (from minimum lag time towards maximum lag time) for the full window at all frequencies, and Fig. 7(d) shows the phase unwrapped along t only around the high weighting area.

The dv/v at different frequencies deduced from phase in Figs 7(b)–(d) are plotted in Fig. 7(e) in green diamonds, orange crosses, and yellow crosses, respectively. The yellow crosses, that is, dv/v measured after accounting for both problems, reconstructs the bold black line (modelled dv/v) well. This accurate measurement of frequency-dependent phase velocity change dv/v can then be inverted to further recover the depth-dependent shear wave velocity changes (Mordret *et al.* 2019).

This example elucidates the usefulness of the wavelet method benefiting from its 2-D representation. Neither of the two issues is easy to resolve with the doublet method, because dt depends on both frequency and lapse-time following the wave dispersion, and cycle skipping generally occurs at different lapse-times for different frequencies. The time-shifts obtained with the wavelet method can be used not only for monitoring applications, but also to determine the misfit that is to be minimized in seismic imaging and tomography (Fichtner *et al*. 2008).

4 INFLUENCE OF SOURCE

The phase of the noise correlation is sensitive to the distribution of noise sources around the stations as well as to their frequency content (e.g. Hadziioannou *et al.* 2009; Yao & Van der Hilst 2009; Weaver *et al.* 2011; Colombi *et al.* 2014). Using single wavelets only, Zhan *et al*. (2013) argued that with the stretching method, temporal variations of the source spectra would produce spurious measurements of wave speed changes. Here we investigate this source effect using coda waves with the stretching, doublet and wavelet methods.

For this purpose, the synthetic coda is generated as before (Section 3.1), except that this time we use the same velocity models but different sources for the reference and current simulations. The inferred velocity change is expected to be zero because the reference and the current velocity models are the same. We examine whether the spurious velocity changes are still observed (due to changes in source spectral content), as suggested by Zhan *et al*. (2013).

The sources for the reference and current simulations are zero-phase Ricker wavelets with widths of 0.106 and 0.089 s, respectively (Fig. 8a). The two phase spectra are identical, but the amplitude spectrum of the current source is that of the reference stretched by 20 per cent (Fig. 8b). The synthetic seismograms are shown in Fig. 8(c), part of the coda in Fig. 8(d), and coda amplitude and phase spectra in Figs 8(e) and (f), respectively. Due to the source difference, the amplitude spectra of two codas have different envelopes (Fig. 8e), with the current coda containing more high-frequency energy than the reference; however, the phase spectra of the two (Fig. 8f) are almost the same.

The dv/v displayed in Fig. 9(a) is calculated using the stretching method, with the optimal stretching ratio determined using a 10 s moving-window. Fig. 9(a) shows that despite the presence of small fluctuations, the measured apparent dv/v is on the order of 10^{-5} at all lapse-times. This is substantially smaller than the values (up to 0.2) observed in Zhan *et al*. (2013), for the same amount of stretching between the current and reference source amplitude spectra.

The fundamental reason for this difference is that Zhan *et al*. (2013) only use single wavelets whereas we use synthetic codas that, effectively, consist of a large number of individual wavelets with random positions and amplitudes. For single wavelets, part of the current waveform (for instance, the side-lobes in Fig. 8a,) is out of phase with the reference. For coda, however, nearly every peak and trough of the current waveform is in phase with the reference's (Fig. 8d). It turns out that the total influence using coda (multiple wavelets) is not simply the sum of effects using each individual wavelet as assumed by Zhan *et al*. (2013), due to changes in sources frequency content. In fact, the source spectral signatures (Fig. 8b) are retained in coda only by the envelopes of the coda spectra (Fig. 8e). The complex oscillations, which essentially characterize the coda spectra, are determined by the scattering properties of the medium. As a result, the peaks and valleys in current and reference spectra (Fig. 8e) almost all occur at the same frequencies. The correlation coefficient between the two spectra, therefore, will in general be maximized with zero stretching of the current trace [eq. (9) in Zhan *et al*. (2013)], suggesting a measurement of zero velocity change.

In principle, the doublet and wavelet methods are based on phase measurements and thus not compromised by changes in source frequency content. This is confirmed by our synthetic experiments . Using both methods, the calculated dt fluctuate around the true value, that is, 0, as a function of lapse time. The fluctuations with the wavelet method are smaller than with the doublet method. The dv/v inferred from linear regressions of dt over t averaged for each frequency bands are shown in Fig. 9(b). It shows that the measured apparent velocity is of the order of 10^{-5} with the doublet method, and even smaller—of the order of 10^{-6}—with the wavelet method. These errors are indicative of the precision limits of the two methods.

Since the dv/v of interest are typically no less than $\sim 10^{-4}$ (Mao *et al*. 2019), spurious dv/v that might result from changes in source amplitude spectra are at least one order smaller than the apparent dv/v measured by the stretching, doublet, or wavelet methods. We thus suggest that the bias in dv/v is negligible for CWI using realistic seismic records, at least for changes in sources frequency content with similar magnitudes as in the tests.

5 A REAL-DATA APPLICATION

To illustrate the performance of the wavelet method we apply it to data from the Salton Sea Geothermal Field (SSGF), California. We compare the measurements using the doublet method (reproduced from Taira *et al*. 2018) and the wavelet method.

Taira *et al*. (2018) investigate the temporal behavior of seismic wavespeed at SSGF using five different frequency bands. We reproduce their results with similar records and processing. The data consist of vertical (ZZ) component ambient seismic noise at eight stations of the CalEnergy network for a period of about 1-yr (15 December 2009 to 1 January 2011) around the 2010 M_w 7.2 El Mayor–Cucapah (EMC)

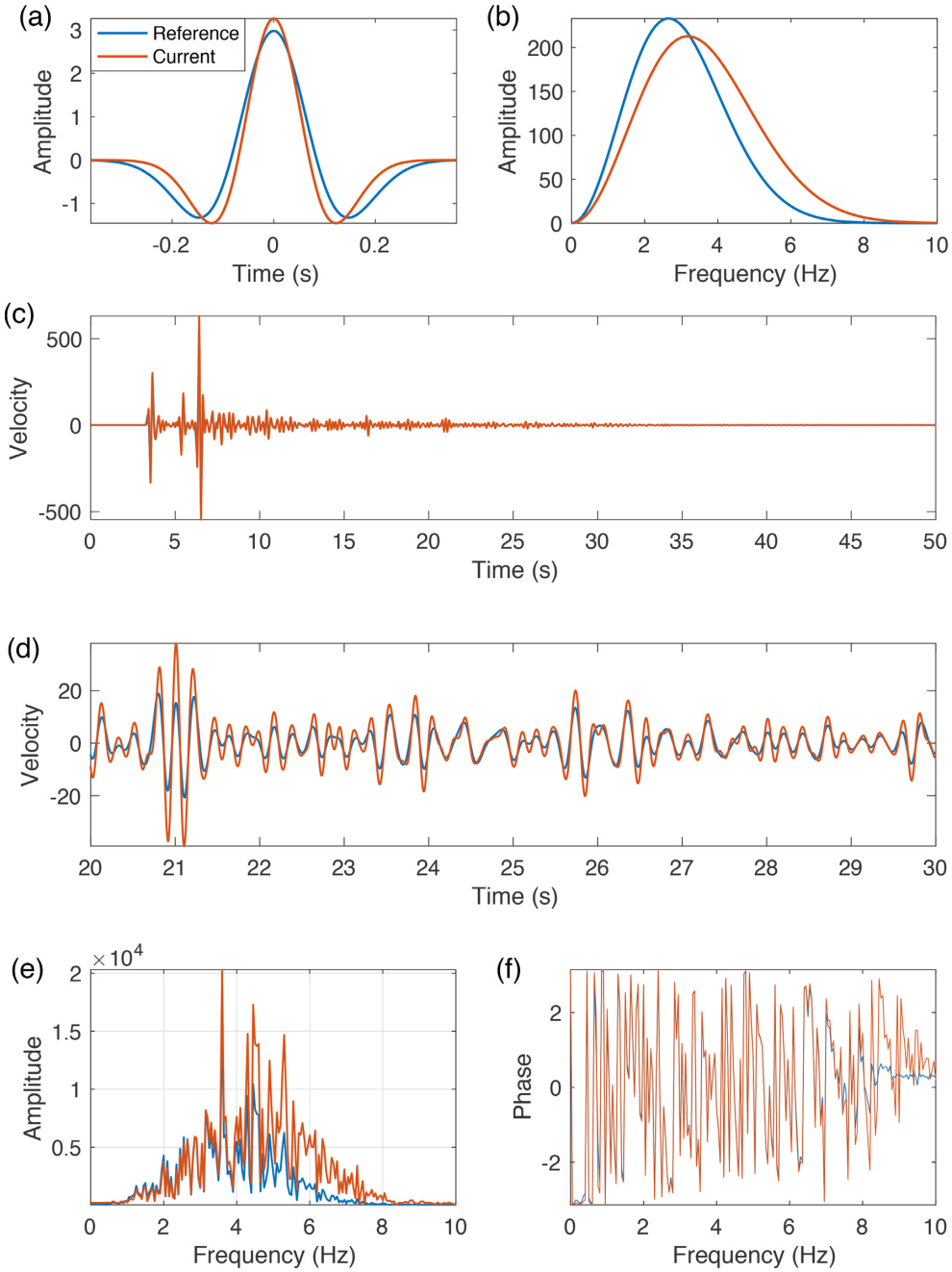

Figure 8. (a) The time-series and (b) the amplitude spectra of the reference and current source wavelets used for investigating source influence on dt measurements as described in Section 4. (c) The synthetic seismograms and (d) a zoom in of the codas. (e) The amplitude spectra and (f) the phase spectra of the synthetic codas from 15 to 35 s.

earthquake. Our results from the doublet method (Fig. 10a) are very similar to the published results in Taira *et al*. (2018), showing that in general dv/v measurements are robust and reproducible. For all five frequency bands, notable and consistent coseismic velocity reductions are observed, followed by a recovery process lasting for several months. With the decreasing of frequency ranges, the magnitudes of the velocity drops increase, indicating larger medium perturbations at larger depth (but no deeper than ∼2.0 km depth).

Before applying the wavelet method, we present a 1-D checker-board type test to assess the performance of different mother wavelets on spectral discrimination. We take a realistic noise cross-correlation trace at SSGF, and stretch or compress it by the same ratio in different frequency bands after bandpass filtering. In this way, we model velocity changes with alternating signs in different frequency bands as in Fig. 11(a), with the expected 2-D time-shifts shown in Fig. 11(b). We then use two different mother wavelets, the Morse (defined in eq. (9) with $[P,\ \gamma] = [3, 10]$, Fig. 2a) and the Morlet wavelet (defined in eq. (7) with $\omega_0 =\ 6$, Fig. 2b], to retrieve the time-shifts. As shown in Figs 12(a) and (b), in general both the Morse and the Morlet wavelets recover the overall pattern of modelled time-shifts with opposite signs in neighboring bands. The Morlet wavelet seems to distinguish better along frequency direction, consistent with Fig. 2. Around the high

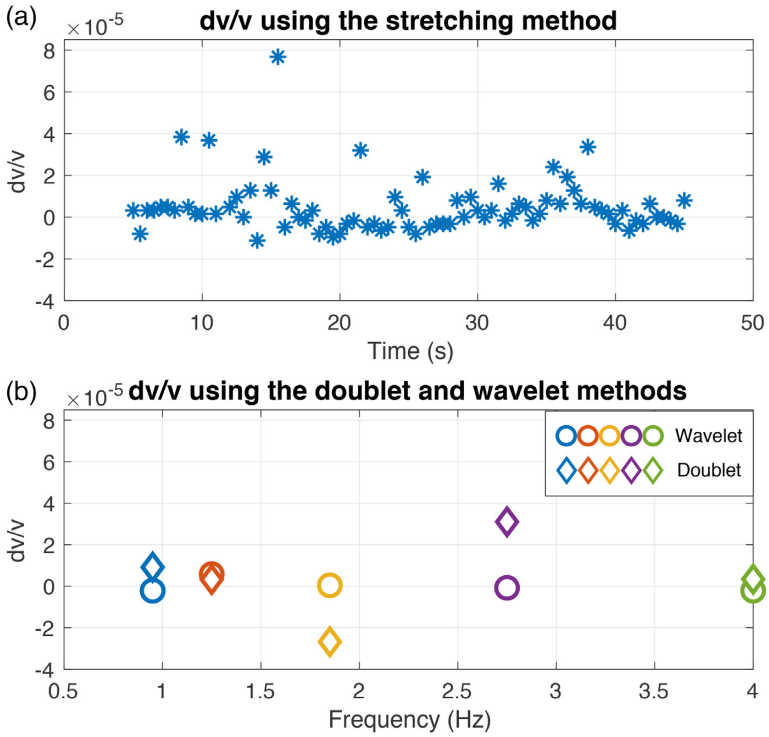

Figure 9. Measurements of d*v*/*v* in synthetic tests incorporating changes in source frequency content but no actual velocity change: (a) using the stretching method at different lapse time and (b) using the doublet method (in coloured diamonds) and the wavelet method (in coloured circles) for different frequency bands.

frequencies, in particular, considerable smearing appears between adjacent frequency bands in d*t* measured with the Morse wavelet (Fig. 12a), whereas with the Morlet wavelet d*t* is less smeared (Fig. 12b).

Now we compare the d*v*/*v* measured using the doublet method (Fig. 10a) to those using the wavelet method—with the Morse wavelet (Fig. 10b) and with the Morlet wavelet (Fig. 10c)—averaged in each frequency bands.

Two features in the results from the doublet method (Fig. 10a) draw our attention. First, measurements in the two lowest frequency bands, 0.5–2.0 Hz and 0.75–3.0 Hz, manifest similar magnitudes of coseismic velocity drops, which would imply that the velocity perturbations due to the big earthquake become rather homogeneous at depth. Using the wavelet method, however, both with the Morse and the Morlet wavelet, the velocity reduction between 0.75 and 3.0 Hz is less than between 0.5 and 2.0 Hz. This suggests (1) that the similarity of d*v*/*v* magnitudes in these frequency bands as measured with the doublet method is an artefact and (2) that the velocity perturbations continue to increase with increasing depth.

Secondly, *dv*/*v* measured in different frequency bands (especially the two highest—1.5–6.0 Hz and 2.0–8.0 Hz) exhibit very similar shapes as a function of time during the recovery process, suggesting uniform patterns of healing, or deformation, at different depths. This characteristic is also apparent in d*v*/*v* computed with the Morse wavelet in the two highest frequency bands but not (or much less so) with the Morlet wavelet. Recall that in the 1-D checker-board test (Fig. 12), strong smearing occurs around high frequencies with the Morse wavelet but not with the Morlet wavelet. This suggests that the similar shapes of d*v*/*v* in the high frequency bands using the doublet method and the wavelet method with the Morse wavelet are most likely due to contamination from adjacent frequencies.

This example demonstrates the wavelet method's reliability in discerning frequency-dependent elastic properties. It also urges caution in interpreting frequency-dependent d*v*/*v* calculated with different methods.

6 DISCUSSIONS

The wavelet method presented in this paper shares some underpinnings with the doublet method. Here we give a comparison between the wavelet and the doublet methods, then discuss the limitations of the wavelet method.

6.1 Comparison of the doublet and the wavelet methods

The basis of the doublet method is to compute local phases by windowed Fourier transform (WFT), whereas the wavelet method calculates local phases by wavelet transform. In this sense, the two methods share the same underlying principle while making use of different tools of time–frequency representation. Nevertheless, the wavelet method has several advantages over the doublet method.

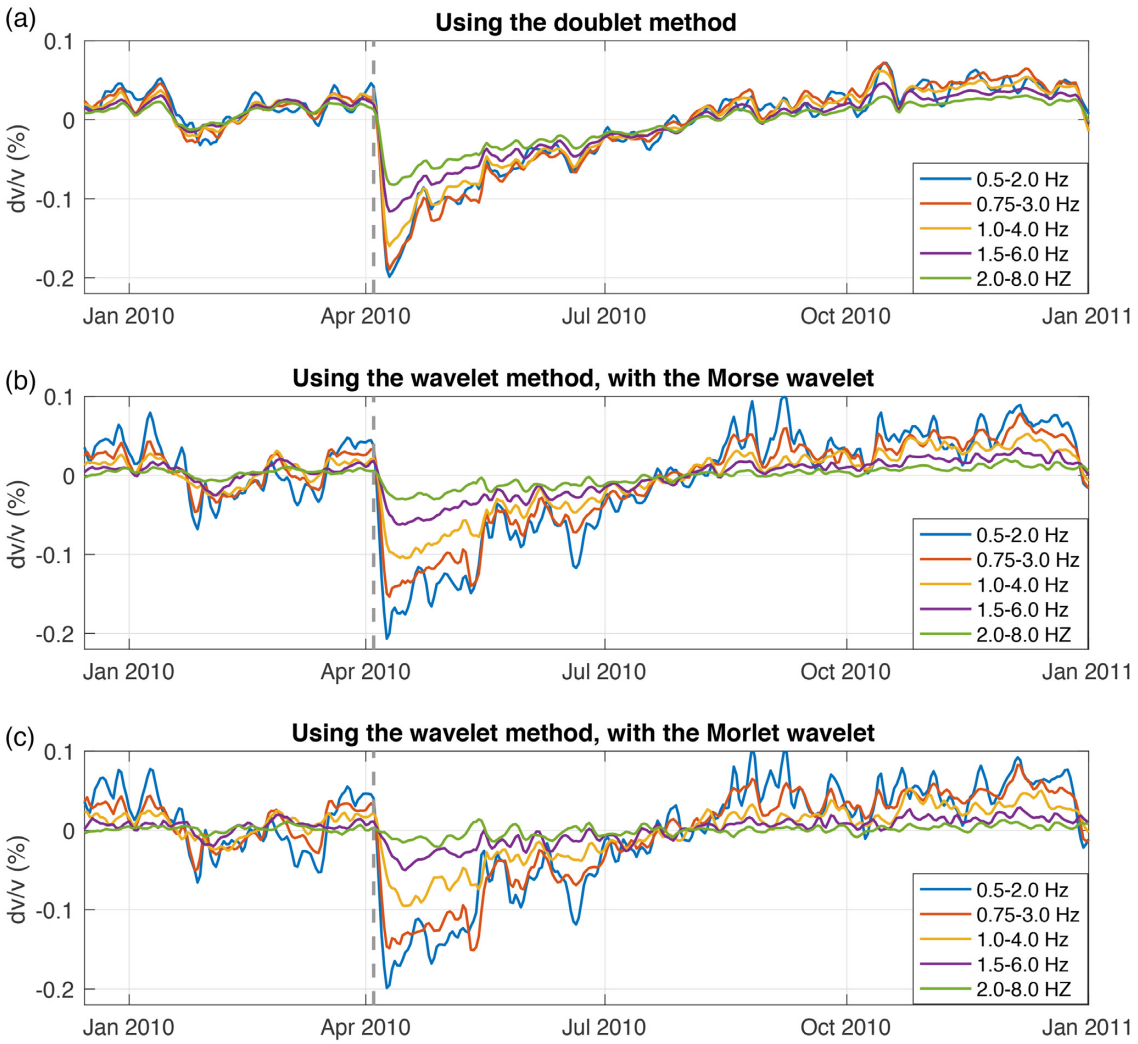

Figure 10. dv/v at Salton Sea Geothermal Field (SSGF) for five frequency bands measured by (a) the doublet method (reproduced from Taira *et al*. 2018), (b) the wavelet method with the Morse wavelet [defined in eq. (9) with $[P,\ \gamma] = [3, 10]$, Fig. 2a] and (c) the wavelet method with the Morlet wavelet [defined in eq. (7) with $\omega_0 = 6$, Fig. 2b]. The vertical dashed line indicates the time of 2010 M_w 7.2 El Mayor-Cucapah earthquake.

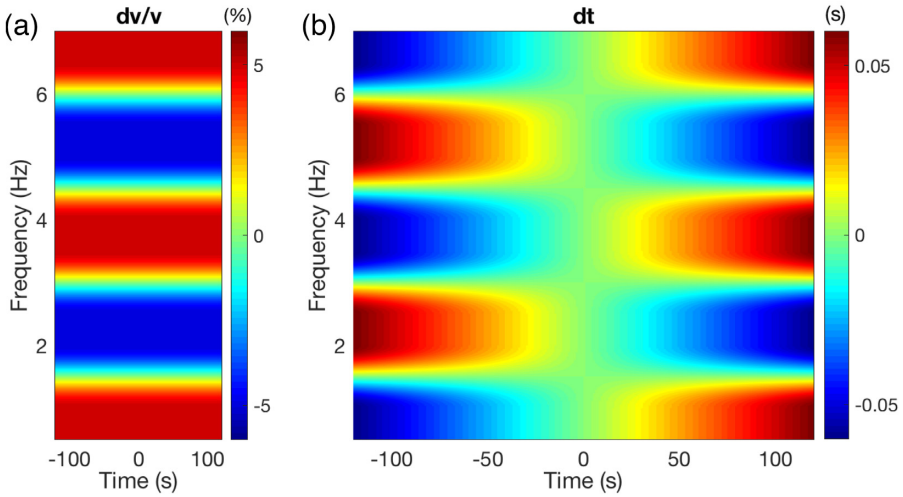

Figure 11. A conceptual illustration of (a) the model dv/v and (b) the expected time-shifts for the 1-D checker-board test.

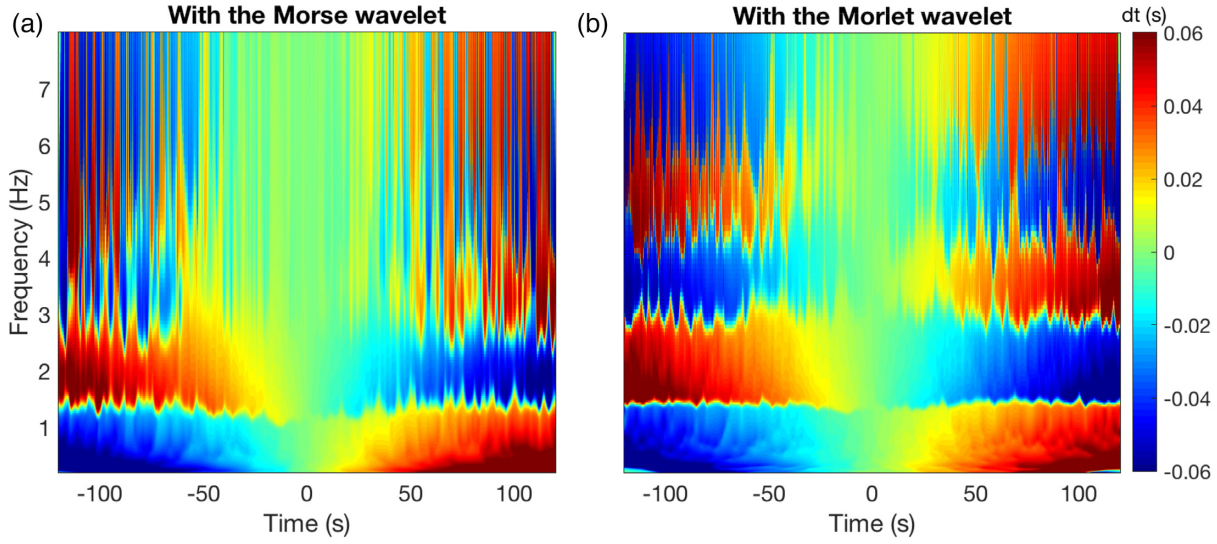

Figure 12. The time difference measured using the wavelet method with (a) the Morse wavelet (defined in eq. (9) with $[P,\ \gamma] = [3, 10]$, Fig. 2a) and (b) the Morlet wavelet (defined in eq. (7) with $\omega_0 = 6$, Fig. 2b) in the 1-D checker-board test.

First, the wavelet method calculates time-shifts over the whole time–frequency domain all at once, which is computationally much more efficient than applying the doublet method to compute WFT in a number of frequency bands. In practice the wavelet transforms can be computed in the spectral domain by exploiting the convolution theorem, which is considerably faster than in time domain.

Secondly, the wavelet method uses a multiresolution strategy, that is, the length of time windows are automatically adapted to each frequency by dilation or compression of the mother wavelet, which naturally and properly provides different time resolutions corresponding to fine features or coarse features of the waveform. The doublet method, however, uses one identical window length for all frequencies within the pre-defined frequency band, and thus only uniform time resolution is used across the whole frequency band.

Thirdly, the wavelet method can deal with dispersive waves, because the 2-D measurements of $\delta t(f,\ t)$ allows the use of a frequency-dependent lapse-time range, with the group velocity dispersion given naturally by the amplitude of wavelet transform (as shown in Section 3.2). Whereas the doublet method has to use the same range for all frequencies within the chosen frequency band. Furthermore, the 2-D representation in the wavelet method allows mitigating the cycle skipping by unwrapping along the lapse-time direction, which is hard to achieve with the doublet method since the phase jumps of different frequencies generally occur at different lapse-times.

Forthly, for both methods, the uncertainty principle requires trade-offs between their inherent time and frequency resolutions. For the wavelet method, this trade-off is determined by the choice of the mother wavelet, and many flexible options that can provide the optimal joint resolution are available. For the doublet method, the trade-off between inherent time and frequency resolutions depends on the window function, and the minimum Heisenberg area is achieved only when the window function is a Gaussian (Mallat 1999). However, with the doublet method, the window function is typically a taper applied to a few percents at the two ends of the window (Brenguier *et al.* 2008a; Lecocq *et al.* 2014) rather than on the whole window. Furthermore, the measurements obtained from the doublet method are average over some predetermined frequency range, which further limits the final frequency resolution permitted by this method.

6.2 Limitations of the wavelet method

In this paper, we have demonstrated that for measuring complicated time- and frequency-dependent shifts in traveltime—and, thus, inhomogeneous velocity changes—the wavelet method is superior to the doublet method. Yet, this method also has limitations.

First, just like the other methods, the reference and the current waveforms need to be similar enough to apply the wavelet method in a meaningful way.

Secondly, measurements of $\phi_{XY}(f,\ t)$ in low power areasof the time-frequency space can be affected and contaminated by the phases in adjacent regions that contain strong power (as in Fig. 5f). Because the spectral resolution of wavelet transform is, although high, not infinite. Applying spectral whitening prior to calculating $\mathrm{d}\,t$ can help stablize the measurements when strong fluctuations of spectral power exist.

Thirdly, the wavelet method can help mitigate the cycle skipping problem to some extent by unwrapping along lapse-time direction (as shown in Section 3.2). This may not work in the late coda if the current waveform differs too much from the reference such that the similarity between the two is lost. In this circumstance, the 2-D phase measurements of the current CWT at larger lapse-time should be shifted to align with the reference prior to calculations of W_{XY} [similar to the modification of the moving-window cross correlation method in Mikesell *et al.* (2015)].

7 CONCLUSIONS

We present a new approach to measure time- and frequency-dependent traveltime changes based on wavelet analysis. With high computational efficiency, this new method gives time-shift measurements over the whole time–frequency space at once. It provides much higher frequency resolution than the traditional methods, and allows flexible trade-offs between time and frequency resolutions with the optimal joint resolution. This wavelet method automatically uses frequency-adaptive time resolutions, and enables the variation of the lapse-time range at different frequencies. With synthetic tests, we demonstrate that the new method can retrieve the traveltime shifts more stably and accurately than the traditional methods. It is also advantageous when dealing with dispersive wave scenarios and in the presence of cycle skippings. An application to real data shows that the wavelet method better separates the dv/v at low frequencies and is less affected by spectral leakage at high frequencies. We also demonstrate that dv/v measurements using the wavelet method and other methods are reasonably insensitive to changes in source frequency content when the measurements are done using coda waves. Our wavelet method shows promise for resolving the spatial distribution of temporal wave speed perturbations and, by implication, for improving our understanding of dynamic processes in the shallow crust.

ACKNOWLEDGEMENTS

The codes for measuring traveltime shifts with the wavelet method proposed in this paper are available at: https://github.com/shujuanmao/dt-wavelet (implemented with the Wavelet Toolbox in Matlab R2018a). Seismic waveform data at Salton Sea Geothermal Field used in this study are avalible through SCEDC. We thank Nori Nakata, Florent Brenguier and Gregor Hillers for insightful discussions, Laurent Demanet and Léonard Seydoux for helpful suggestions on CWT, and Dunzhu Li for sharing the 2-D Finite Difference code. We also thank Frederik Simons and an anonymous reviewer for their thorough feedbacks. This project has received funding from the European Research Council (ERC) under the European Union's Horizon 2020 Research and Innovation Program (grant agreement N° 742335, F-IMAGE). Aurélien Mordret acknowledges the U.S. National Science Foundation (NSF) Grant PLR-1643761.

REFERENCES

Baker, J.W., 2007. Quantitative classification of near-fault ground motions using wavelet analysis, *Bull. seism. Soc. Am.,* **97,** 1486–1501.

Brenguier, F., Campillo, M., Hadziioannou, C., Shapiro, N.M., Nadeau, R.M. & Larose, E., 2008b. Postseismic relaxation along the San Andreas fault at Parkfield from continuous seismological observations, *Science,* **321,** 1478–1481.

Brenguier, F., Campillo, M., Takeda, T., Aoki, Y., Shapiro, N.M., Briand, X., Emoto, K. & Miyake, H., 2014. Mapping pressurized volcanic fluids from induced crustal seismic velocity drops, *Science,* **345,** 80–82.

Brenguier, F. *et al.*, 2019. Noise-based ballistic body-wave passive seismic monitoring – Part1: Body-waves, *Geophys. J. Int.,* accepted.

Brenguier, F., Shapiro, N.M., Campillo, M., Ferrazzini, V., Duputel, Z., Coutant, O. & Nercessian, A., 2008a. Towards forecasting volcanic eruptions using seismic noise, *Nat. Geosci.,* **1,** 126–130.

Chen, J.H., Froment, B., Liu, Q.Y. & Campillo, M., 2010. Distribution of seismic wave speed changes associated with the 12 May 2008 Mw 7.9 Wenchuan earthquake, *Geophys. Res. Lett.,* **37,** doi:10.1029/2010GL044582.

Clarke, D., Zaccarelli, L., Shapiro, N.M. & Brenguier, F., 2011. Assessment of resolution and accuracy of the Moving Window Cross Spectral technique for monitoring crustal temporal variations using ambient seismic noise, *Geophys. J. Int.,* **186,** 867–882.

Clements, T. & Denolle, M.A., 2018. Tracking groundwater levels using the ambient seismic field, *Geophys. Res. Lett.,* **45,** 6459–6465.

Colombi, A., Chaput, J., Brenguier, F., Hillers, G., Roux, P. & Campillo, M.(2014) On the temporal stability of the coda of ambient noise correlations, *Comptes Rendus - Geosci.,* **346,** 307–316.

Daubechies, I., 1992. *Ten Lectures on Wavelets,* Vol. **61**, SIAM.

De Ridder, S.A.L., Biondi, B.L. & Clapp, R.G., 2014. Time-lapse seismic noise correlation tomography at Valhall, *Geophys. Res. Lett.,* **41,** 6116–6122.

Fang, H. & Zhang, H., 2014. Wavelet-based double difference seismic tomography with sparsity regularization, *Geophys. J. Int.,* **199**(2), 944–955.

Farge, M., 1992. Wavelet transforms and their applications to turbulence, *Annu. Rev. Fluid Mech.,* **24,** 395–458.

Fichtner, A., Kennett, B.L.N., Igel, H. & Bunge, H.P., 2008. Theoretical background for continental- and global-scale full-waveform inversion in the time–frequency domain, *Geophys. J. Int.,* **175,** 665–685.

Frankel, A. & Clayton, R.W., 1986. Finite difference simulations of seismic scattering: implications for the propagation of short-period seismic waves in the crust and models of crustal heterogeneity, *J. geophys. Res.,* **91,** 6465.

Froment, B., Campillo, M., Chen, J.H. & Liu, Q.Y., 2013. Deformation at depth associated with the 12 May 2008 MW 7.9 Wenchuan earthquake from seismic ambient noise monitoring, *Geophys. Res. Lett.,* **40,** 78–82.

Fréchet, J., Martel, L., Nikolla, L. & Poupinet, G., 1989. Application of the cross-spectral moving-window technique (CSMWT) to the seismic monitoring of forced fluid migration in a rock mass, *Int. J. Rock Mech. Min. Sci.,* **26,** 221–233.

Gao, J., Dong, X., Wang, W.B., Li, Y. & Pan, C., 1999. Instantaneous parameters extraction via wavelet transform, *IEEE Trans. Geosci. Remote Sens.,* **37,** 867–870.

Gardner, G.H.F., Gardner, L.W. & Gregory, A.R., 1974. Formation velocity and density—the diagnostic basis for stratigraphic traps, *Geophysics,* **39,** 770–780.

Grinsted, A., Moore, J.C. & Jevrejeva, S., 2004. Application of the cross wavelet transform and wavelet coherence to geophysical time series, *Nonlin. Process. Geophys.,* **11,** 561–566.

Hadziioannou, C., Larose, E., Coutant, O., Roux, P. & Campillo, M., 2009. Stability of monitoring weak changes in multiply scattering media with ambient noise correlation: laboratory experiments, *J. acoust. Soc. Am.,* **125,** 3688–3695.

Hillers, G., Ben-Zion, Y., Campillo, M. & Zigone, D., 2015b. Seasonal variations of seismic velocities in the San Jacinto fault area observed with ambient seismic noise, *Geophys. J. Int.,* **202,** 920–932.

Hillers, G., Campillo, M. & Ma, K.F., 2014. Seismic velocity variations at TCDP are controlled by MJO driven precipitation pattern and high fluid discharge properties, *Earth planet. Sci. Lett.,* **391,** 121–127.

Hillers, G., Husen, S., Obermann, A., Planès, T., Larose, E. & Campillo, M., 2015a. Noise-based monitoring and imaging of aseismic transient deformation induced by the 2006 Basel reservoir stimulation, *Geophysics,* **80,** KS51–KS68.

Hobiger, M., Wegler, U., Shiomi, K. & Nakahara, H., 2012. Coseismic and postseismic elastic wave velocity variations caused by the

2008 Iwate-Miyagi Nairiku earthquake, Japan, *J. geophys. Res.,* **117,** doi:10.1029/2012JB009402.

Kanu, C. & Snieder, R., 2015. Numerical computation of the sensitivity kernel for monitoring weak changes with multiply scattered acoustic waves, *Geophys. J. Int.,* **203,** 1923–1936.

Kristeková, M., Kristek, J., Moczo, P. & Day, S.M., 2006. Misfit criteria for quantitative comparison of seismograms, *Bull. seism. Soc. Am.,* **96,** 1836–1850.

Larose, E., Planes, T., Rossetto, V. & Margerin, L., 2010. Locating a small change in a multiple scattering environment, *Appl. Phys. Lett.,* **96,** doi:10.1063/1.3431269.

Leary, P.C., Malin, P.E., Phinney, R.A., Brocher, T. & VonColln, R., 1979. Systematic monitoring of millisecond travel time variations near Palmdale, California, *J. geophys. Res.,* **84,** 659.

Lecocq, T., Caudron, C. & Brenguier, F., 2014. Msnoise, a python package for monitoring seismic velocity changes using ambient seismic noise, *Seismol. Res. Lett.,* **85,** 715–726.

Lecocq, T., Longuevergne, L., Pedersen, H.A., Brenguier, F. & Stammler, K., 2017. Monitoring ground water storage at mesoscale using seismic noise: 30 years of continuous observation and thermo-elastic and hydrological modeling, *Sci. Rep.,* **7,** 14241.

Li, D., Helmberger, D., Clayton, R.W. & Sun, D., 2014. Global synthetic seismograms using a 2-D finite-difference method, *Geophys. J. Int.,* **197,** 1166–1183.

Lilly, J.M. & Olhede, S.C., 2009. Higher-order properties of analytic wavelets, *IEEE Trans. Signal Process.,* **57,** 146–160.

Liu, P.C., 1994. Wavelet spectrum analysis and ocean wind waves, in *Wavelet Analysis and Its Applications,* Vol. **4,** pp. 151–166, World Scientific, doi:10.1016/B978-0-08-052087-2.50012-8.

Lobkis, O.I. & Weaver, R.L., 2003. Coda-wave interferometry in finite solids: recovery of P-to-S conversion rates in an elastodynamic billiard, *Phys. Rev. Lett.,* **90,** 4.

Mallat, S., 1999. *A Wavelet Tour of Signal Processing,* Elsevier, doi:10.1016/B978-0-12-466606-1.X5000-4.

Mao, S., Campillo, M., Van der Hilst, R.D., Brenguier, F., Stehly, L. & Hillers, G., 2019. High temporal resolution monitoring of small variations in crustal strain by dense seismic arrays, *Geophys. Res. Lett.,* **46,** 128–137.

Margerin, L., Planès, T., Mayor, J. & Calvet, M., 2016. Sensitivity kernels for coda-wave interferometry and scattering tomography: theory and numerical evaluation in two-dimensional anisotropically scattering media, *Geophys. J. Int.,* **204,** 650–666.

Mayor, J., Margerin, L. & Calvet, M., 2014. Sensitivity of coda waves to spatial variations of absorption and scattering: radiative transfer theory and 2-D examples, *Geophys. J. Int.,* **197,** 1117–1137.

Meyers, S.D., Kelly, B.G. & O'Brien, J.J., 1993. An introduction to wavelet analysis in oceanography and meteorology: with application to the dispersion of yanai waves, *Mon. Weather Rev.,* **121,** .

Mikesell, T.D., Malcolm, A.E., Yang, D. & Haney, M.M., 2015. A comparison of methods to estimate seismic phase delays: numerical examples for coda wave interferometry, *Geophys. J. Int.,* **202,** 347–360.

Mordret, A., Jolly, A.D., Duputel, Z. & Fournier, N., 2010. Monitoring of phreatic eruptions using Interferometry on Retrieved Cross-Correlation function from ambient seismic noise: results from Mt. Ruapehu, New Zealand, *J. Volc. Geotherm. Res.,* **191,** 46–59.

Mordret, A., Mikesell, T.D., Harig, C., Lipovsky, B.P. & Prieto, G.A., 2016. Monitoring southwest Greenland's ice sheet melt with ambient seismic noise, *Sci. Adv.,* **2,** 1–9.

Mordret, A., Shapiro, N.M. & Singh, S., 2014. Seismic noise-based time-lapse monitoring of the Valhall overburden, *Geophys. Res. Lett.,* **41,** 4945–4952.

Mordret, A. *et al.* 2020. Noise-based ballistic wave passive seismic monitoring – Part 2. Surface waves, *Geophys. J. Int.,* accepted.

Morlet, J., Arens, G., Fourgeau, E. & Giard, D., 1982a. Wave propagation and sampling theory – Part I. Complex signal and scattering in multilayered media, *Geophysics,* **47,** 203–221.

Morlet, J., Arens, G., Fourgeau, E. & Giard, D., 1982b. Wave propagation and sampling theory – Part II. Sampling theory and complex waves, *Geophysics,* **47,** 222–236.

Niu, F., Silver, P.G., Daley, T.M., Cheng, X. & Majer, E.L., 2008. Preseismic velocity changes observed from active source monitoring at the Parkfield SAFOD drill site, *Nature,* **454,** 204–208.

Niu, F., Silver, P.G., Nadeau, R.M. & McEvilly, T. V., 2003. Migration of seismic scatterers associated with the 1993 Parkfield aseismic transient event, *Nature,* **426,** 544–548.

Obermann, A., Planès, T., Larose, E. & Campillo, M., 2019. 4-D Imaging of subsurface changes with coda waves: numerical studies of 3-D combined sensitivity kernels and applications to the Mw 7.9, 2008 Wenchuan Earthquake, *Pure appl. Geophys.,* **176,** 1243–1254.

Obermann, A., Planès, T., Larose, E., Sens-Schönfelder, C. & Campillo, M., 2013. Depth sensitivity of seismic coda waves to velocity perturbations in an elastic heterogeneous medium, *Geophys. J. Int.,* **194,** 372–382.

Obermann, A., Planés, T., Hadziioannou, C. & Campillo, M., 2016. Lapse-time-dependent coda-wave depth sensitivity to local velocity perturbations in 3-D heterogeneous elastic media, *Geophys. J. Int.,* **207,** 59–66.

Olivier, G., Brenguier, F., Campillo, M., Lynch, R. & Roux, P., 2015. Body-wave reconstruction from ambient seismic noise correlations in an underground mine, *Geophysics,* **80,** KS11–KS25.

Pacheco, C. & Snieder, R., 2005. Time-lapse travel time change of multiply scattered acoustic waves, *J. acoust. Soc. Am.,* **118,** 1300–1310.

Peng, Z. & Ben-Zion, Y., 2006. Temporal changes of shallow seismic velocity around the Karadere-Düzce branch of the north Anatolian fault and strong ground motion, *Pure appl. Geophys.,* **163,** 567–600.

Planès, T., Larose, E., Margerin, L., Rossetto, V. & Sens-Schönfelder, C., 2014. Decorrelation and phase-shift of coda waves induced by local chages: multiple scattering approach and numerical validation, *Waves in Random and Complex Media,* **24**(2), 99–125.

Poupinet, G., Ellsworth, W.L. & Frechet, J., 1984. Monitoring velocity variations in the crust using earthquake doublets: an application to the Calaveras Fault, California, *J. geophys. Res.,* **89,** 5719–5731.

Ratdomopurbo, A. & Poupinet, G., 1995. Monitoring a temporal change of seismic velocity in a volcano: application to the 1992 eruption of Mt. Merapi (Indonesia), *Geophys. Res. Lett.,* **22,** 775–778.

Reasenberg, P. & Aki, K., 1974. A precise, continuous measurement of seismic velocity for monitoring in situ stress, *J. geophys. Res.,* **79,** 399–406.

Rivet, D., Brenguier, F. & Cappa, F., 2015. Improved detection of preeruptive seismic velocity drops at the Piton de la Fournaise volcano, *Geophys. Res. Lett.,* **42,** 6332–6339.

Rivet, D., Campillo, M., Shapiro, N.M., Cruz-Atienza, V., Radiguet, M., Cotte, N. & Kostoglodov, V., 2011. Seismic evidence of nonlinear crustal deformation during a large slow slip event in Mexico, *Geophys. Res. Lett.,* **38,** 3–7.

Rivet, D. *et al.*, 2013. Seismic velocity changes, strain rate and non-volcanic tremors during the 2009–2010 slow slip event in Guerrero, Mexico, *Geophys. J. Int.,* **196,** 447–460.

Roberts, P.M., Scott Phillips, W. & Fehler, M.C., 1992. Development of the active doublet method for measuring small velocity and attenuation changes in solids, *J. acoust. Soc. Am.,* **91,** 3291–3302.

Rubinstein, J.L., Uchida, N. & Beroza, G.C., 2007. Seismic velocity reductions caused by the 2003 Tokachi-Oki earthquake, *J. geophys. Res.,* **112,** doi:10.1029/2006JB004440.

SCEDC, Southern California Earthquake Data Center, Dataset, 2013. http://scedc.caltech.edu.

Schaff, D.P. & Beroza, G.C., 2004. Coseismic and postseismic velocity changes measured by repeating earthquakes, *J. geophys. Res.,* **109,** doi:10.1029/2004JB003011.

Sens-Schönfelder, C. & Eulenfeld, T., 2019. Probing the in situ elastic nonlinearity of rocks with earth tides and seismic noise, *Phys. Rev. Lett.,* **122,** 138501.

Sens-Schönfelder, C. & Wegler, U., 2006. Passive image interferemetry and seasonal variations of seismic velocities at Merapi Volcano, Indonesia, *Geophys. Res. Lett.,* **33,** 1–5.

Shapiro, N.M. & Campillo, M., 2004. Emergence of broadband Rayleigh waves from correlations of the ambient seismic noise, *Geophys. Res. Lett.,* **31,** doi:10.1029/2004GL019491.

Snieder, R., 2006. The theory of coda wave interferometry, *Pure appl. Geophys.,* **163,** 455–473.

Snieder, R., Grêt, A., Douma, H. & Scales, J., 2002. Coda wave interferometry for estimating nonlinear behavior in seismic velocity, *Science,* **295,** 2253–2255.

Taira, T., Avinash, N., Brenguier, F. & Manga, M., 2018. Monitoring reservoir response to earthquakes and fluid extraction, salton sea geothermal field, California, *Sci. Adv.,* **4,** doi:10.1126/sciadv.1701536.

Torrence, C. & Compo, G.P., 1998. A practical guide to wavelet analysis, *Bull. Am. Meteorol. Soc.,* **79,** 61–78.

Torrence, C. & Webster, P.J., 1999. Interdecadal changes in the ENSO–Monsoon system, *J. Clim.,* **12,** 2679–2690.

Toyokuni, G., Takenaka, H., Takagi, R., Kanao, M., Tsuboi, S., Tono, Y., Childs, D. & Zhao, D., 2018. Changes in Greenland ice bed conditions inferred from seismology, *Phys. Earth planet. Inter.,* **277,** 81–98.

Vidale, J.E. & Li, Y.G., 2003. Damage to the shallow Landers fault from the nearby Hector Mine earthquake, *Nature,* **421,** 524–526.

Wang, B., Zhu, P., Chen, Y., Niu, F. & Wang, B., 2008. Continuous subsurface velocity measurement with coda wave interferometry, *J. geophys. Res.,* **113,** 1–12.

Wang, Q.Y., Brenguier, F., Campillo, M., Lecointre, A., Takeda, T. & Aoki, Y., 2017. Seasonal crustal seismic velocity changes throughout Japan, *J. geophys. Res.,* **122,** 7987–8002.

Weaver, R., Froment, B. & Campillo, M., 2009. On the correlation of non-isotropically distributed ballistic scalar diffuse waves, *J. acoust. Soc. Am.,* **126,** 1817.

Weaver, R.L., Hadziioannou, C., Larose, E. & Campillo, M., 2011. On the precision of noise correlation interferometry, *Geophys. J. Int.,* **185,** 1384–1392.

Wegler, U., Nakahara, H., Sens-Schönfelder, C., Korn, M. & Shiomi, K., 2009. Sudden drop of seismic velocity after the 2004 Mw 6.6 mid-Niigata earthquake, Japan, observed with Passive Image Interferometry B06305, *J. geophys. Res.,* **114,** doi:10.1029/2008JB005869.

Wu, C., Delorey, A., Brenguier, F., Hadziioannou, C., Daub, E. G. & Johnson, P., 2016. Constraining depth range of S wave velocity decrease after large earthquakes near Parkfield California, *Geophys. Res. Lett.,* **43**(12), 6129–6136.

Yamamura, K., Sano, O., Utada, H., Takei, Y., Nakao, S. & Fukao, Y., 2003. Long-term observation of in situ seismic velocity and attenuation, *J. geophys. Res.,* **108,** 1–15.

Yao, H. & Van der Hilst, R.D., 2009. Analysis of ambient noise energy distribution and phase velocity bias in ambient noise tomography, with application to SE Tibet, *Geophys. J. Int.,* **179,** 1113–1132.

Yao, H., Van der Hilst, R.D. & De Hoop, M. V., 2006. Surface-wave array tomography in SE Tibet from ambient seismic noise and two-station analysis - I. Phase velocity maps, *Geophys. J. Int.,* **166,** 732–744.

Yomogida, K., 1994. Detection of anomalous seismic phases by the wavelet transform, *Geophys. J. Int.,* **116,** 119–130.

Zhan, Z., Tsai, V.C. & Clayton, R.W., 2013. Spurious velocity changes caused by temporal variations in ambient noise frequency content, *Geophys. J. Int.,* **194,** 1574–1581.